

Banner appropriate to article type will appear here in typeset article

# Influences of small-scale shear instability on passive scalar mixing in a shear-free turbulent front

Tomoaki Watanabe<sup>1</sup>† Koji Nagata<sup>1</sup>

<sup>1</sup>Department of Mechanical Engineering and Science, Kyoto University, Kyoto 615-8540, Japan

(Received xx; revised xx; accepted xx)

This version (accepted manuscript) is free to view and download for private research and study only. The final version is available on <https://doi.org/10.1017/jfm.2025.88>.

Local shearing motions in turbulence form small-scale shear layers, which are unstable to perturbations at approximately 30 times the Kolmogorov scale. This study conducts direct numerical simulations of passive-scalar mixing layers in a shear-free turbulent front to investigate mixing enhancements induced by such perturbations. The initial turbulent Reynolds number based on the Taylor microscale is  $Re_\lambda = 72$  or 202. The turbulent front develops by entraining outer fluid. Weak sinusoidal velocity perturbations are introduced locally, either inside or outside the turbulent front, or globally throughout the flow. Perturbations at this critical wavelength promote small-scale shear instability, complicating the boundary geometry of the scalar mixing layer at small scales. This increases the fractal dimension and enhances scalar diffusion outward from the scalar mixing layer. Additionally, the promoted instability increases the scalar dissipation rate and turbulent scalar flux at small scales, facilitating faster scalar mixing. The effects manifest locally; external perturbations intensify mixing near the boundary, while internal perturbations affect the entire turbulent region. The impact of perturbations is consistent across different Reynolds numbers when the amplitudes normalised by the Kolmogorov velocity are the same, indicating that even weaker perturbations can enhance scalar mixing at higher Reynolds numbers. The mean scalar dissipation rate increases by up to 50%, even when the perturbation energy is only 2.5% of the turbulent kinetic energy. These results underscore the potential to leverage small-scale shear instability for efficient mixing enhancement in applications such as chemically reacting flows.

## 1. Introduction

Turbulent mixing is a pivotal process in various engineering and environmental flows. The fluid motions within turbulence effectively facilitate the transport and diffusion of scalars such as species concentration and heat. In chemical processes, the rapid molecular-level mixing induced by turbulent motions markedly influences the progression of reactions (Hill 1976; Fox 2003). Elucidating this turbulent mixing process is crucial for modelling and controlling scalar transport in practical applications. The simplest scenario involves the mixing of a

† Email address for correspondence: [watanabe.tomoaki.8x@kyoto-u.ac.jp](mailto:watanabe.tomoaki.8x@kyoto-u.ac.jp)

passive scalar, which does not influence the velocity fields. Examples include the mixing of gases with identical densities, the diffusion of dilute dye solutions and heat transfer involving minimal temperature differences. Mixing of passive scalars has been extensively explored in prior studies of turbulent mixing (Dimotakis 2005).

Turbulence is frequently studied with a focus on coherent structures, defined by their characteristic flow patterns. At small scales, these structures, characterised by vorticity, often take tubular or sheet-like geometries. The tubular structures are vortex tubes, responsible for local fluid motions of rigid-body rotation (Siggia 1981; Jiménez & Wray 1998; Kolář 2007). The sheet-like regions with vorticity relate to local shearing motions, and the associated structures are referred to as vortex sheets or simply shear layers (Ruetsch & Maxey 1991; Eisma *et al.* 2015). The present study calls them shear layers because their essential characteristic is shear rather than vorticity. It is important to note that the shear layers discussed here are associated with velocity fluctuations, whereas a large-scale shear layer, observed in the initial laminar regime of a mixing layer, relates to the mean velocity distribution (Papamoschou & Roshko 1988). Vortex tubes have garnered more attention in past studies, evidenced by numerous publications (Siggia 1981; Jiménez *et al.* 1993; Jiménez & Wray 1998; Mouri *et al.* 2007; Kang *et al.* 2007; da Silva *et al.* 2011; Jahanbakhshi *et al.* 2015; Ghira *et al.* 2022). These studies often utilise conditional averaging techniques, analysing the mean flow pattern around specific flow regions (Antonia 1981). Vortex tubes are small-scale structures, with length scales on the order of the Kolmogorov scale, and experience strain that leads to vortex stretching. The relationship between strain and tube diameter in turbulence aligns well with Burgers' vortex model, which represents one of the few exact steady solutions of the Navier–Stokes equations.

In contrast, shear layers have received less investigative focus. Unlike the statistical analysis based on conditional averages for vortex tubes, most investigations into shear layers have relied on visualisation or analysing flow regions occupied by shear layers (Ruetsch & Maxey 1992; Vincent & Meneguzzi 1994; Horiuti & Takagi 2005; Pirozzoli *et al.* 2010; Buxton & Ganapathisubramani 2010; Bhatt & Tsuji 2021). This is likely due to the classical identification scheme of shear layers focusing on their location without information on orientations, crucial for conditional analysis. However, recent advancements in shear layer identification have significantly propelled the study of these structures, beginning with investigations into a turbulent boundary layer (Eisma *et al.* 2015). These studies employ a new decomposition of the velocity gradient tensor, extracting a shear component. Such decompositions include the triple decomposition, Rortex-based decomposition and Shur decomposition, which are related to each other although the calculation algorithms are different (Kolář 2007; Liu *et al.* 2018; Kronborg & Hoffman 2023). Over the past decade, many characteristics of shear layers have been revealed. They are the smallest scale structures in turbulence, with their length and velocity scales determined by the Kolmogorov scales both in isotropic turbulence and free shear flows (Watanabe *et al.* 2020; Fiscaletti *et al.* 2021; Hayashi *et al.* 2021a). These studies have demonstrated that the mean thickness and velocity jump of shear layers, normalised by the Kolmogorov scales, remain constant with respect to the turbulent Reynolds number  $Re_\lambda$ , based on the Taylor microscale, for low to moderately large  $Re_\lambda$ . In forced isotropic turbulence, the normalised thickness and velocity jump exhibit quantitative consistency across  $Re_\lambda \approx 40$  to 300, despite  $Re_\lambda \approx 40$  being insufficiently large to observe the inertial subrange (Watanabe *et al.* 2020). Shear layers in turbulence also resemble Burgers' vortex layer, forming within a straining flow with compression in the layer-normal direction and extension in the shear-vorticity direction (Watanabe *et al.* 2020). The shear layers and the velocity fields they induce are essential in various properties of turbulence, such as energy cascades, enstrophy production and momentum and scalar transports (Pirozzoli *et al.* 2010;

Enoki *et al.* 2023). It should be noted that similar layer structures have also been reported in the mean flow field observed within a strain eigenframe (Elsinga & Marusic 2010; Elsinga *et al.* 2017; Sakurai & Ishihara 2018). This observation can be explained by the predominance of shearing motion almost everywhere in turbulence (Nagata *et al.* 2020a; Das & Girimaji 2020).

In addition to the shear layers at the smallest scale of turbulent motions, similar shear layers exist across various length scales. Experiments on decaying isotropic turbulence with  $400 \lesssim Re_\lambda \lesssim 900$  have demonstrated that shear layer structures spanning a wide range of scales within the inertial subrange exhibit self-similarity, with the scale dependence of the mean velocity jump predicted by Kolmogorov’s second similarity hypothesis (Watanabe *et al.* 2024). Shear layers at the smallest scale have a mean thickness of approximately 4–5 times the Kolmogorov scale, whereas velocity distributions in turbulence, observed through both direct numerical simulations (DNSs) and experiments, often reveal shear regions with thicknesses significantly larger than the Kolmogorov scale (Ishihara *et al.* 2013; Heisel *et al.* 2021; Fiscaletti *et al.* 2022). These shear regions identified in velocity profiles are likely related to shear layers at intermediate scales larger than the Kolmogorov scale.

One of the important dynamical properties of shear layers is their instability. As they evolve, shear layers are inherently unstable and prone to collapse. This instability leads to the formation of vortex tubes, as already observed in early flow visualisation studies (Vincent & Meneguzzi 1994; Passot *et al.* 1995). Recent studies have elucidated a mean flow pattern around shear layers (Watanabe *et al.* 2020; Fiscaletti *et al.* 2021), leading to the development of a simple model of shear layers in turbulence. Numerical simulations of this model demonstrate that a shear layer with a small aspect ratio is unstable due to self-induced velocity even without perturbations (Watanabe & Nagata 2023). This contrasts with the Kelvin–Helmholtz instability observed in a uniform shear layer with an infinite aspect ratio, which remains stable without perturbations. The vortex formation process from a shear layer with a finite aspect ratio is accelerated under the influence of velocity perturbations of a specific wavelength. These observations indicate that many shear layers in turbulent flows become unstable by perturbations with a wavelength approximately 30 times the Kolmogorov scale, regardless of the Reynolds number. This critical wavelength was determined using the most unstable wavelength of the shear layer model and the thickness of the shear layers in isotropic turbulence. The impacts of such perturbations on shear layers have been investigated through DNS of decaying isotropic turbulence with  $40 \lesssim Re_\lambda \lesssim 130$  (Watanabe & Nagata 2023). Perturbations near this critical wavelength excite the instability of many shear layers, resulting in a higher number density of vortices. Consequently, small-scale turbulent motions become more active, leading to an increased rate of turbulent kinetic energy dissipation, as well as enhanced enstrophy and strain amplifications. However, perturbations with a much larger wavelength, such as more than 100 times the Kolmogorov scale, do not affect the evolution of shear layers, and the increase in vortices due to promoted shear instability does not occur. The increase ratio in vortices resulting from perturbations with a wavelength of approximately 30 times the Kolmogorov scale remains quantitatively consistent across different Reynolds numbers when the perturbation amplitude normalised by the Kolmogorov velocity is fixed. Vortices increase more as the normalised amplitude becomes larger.

The perturbation-induced instability of small-scale shear layers can be leveraged using weak disturbances to modulate turbulence. Similar strategies, based on other flow instabilities associated with large-scale characteristics defined by the mean flow distribution, have proven effective in previous studies (Cattafesta III & Sheplak 2011). One example is the initial instability of a jet near a nozzle, which can be manipulated to enhance or suppress jet development and concurrent scalar mixing (Longmire *et al.* 1992; Zaman *et al.* 1994; Benard *et al.* 2008; Ito *et al.* 2018). This approach involves the manipulation of

the turbulent transition process at large scales, while the small-scale shear instability considered in this study occurs in a fully-developed turbulent region, which is, in the example case of the jet, a downstream region far from the nozzle. Therefore, these two approaches, involving large- and small-scale instabilities, are not competitive but can be complementarily used together in practical applications. The concept of utilising small-scale shear instability is relatively new but has been tested for turbulent entrainment, a pivotal process in which nearby non-turbulent fluid is drawn into a turbulent region. This phenomenon is observed in canonical turbulent flows such as jets, mixing layers and wakes (da Silva *et al.* 2014). Local entrainment in various flows occurs at small scales within a thin interface layer, known as the turbulent/non-turbulent interface (TNTI) layer (Holzner & Lüthi 2011; Wolf *et al.* 2012; Taveira & da Silva 2014; van Reeuwijk & Holzner 2014; Watanabe *et al.* 2016c; Jahanbakhshi & Madnia 2016). Many vortex tubes and shear layers exist within the TNTI layer, influencing the entrainment process by drawing non-turbulent fluid into these structures and facilitating outward vorticity diffusion from their cores (da Silva *et al.* 2011; Jahanbakhshi *et al.* 2015; Watanabe *et al.* 2017; Neamtu-Halic *et al.* 2020; Hayashi *et al.* 2021b). DNSs of a localised turbulent region have shown that when weak velocity perturbations with the unstable wavelength of small-scale shear layers are introduced into the turbulence, shear layers near the TNTI layer rapidly collapse, forming vortex tubes (Watanabe 2024a). This effect on shear layers results in an enhanced entrainment rate. Such an increase in the entrainment rate does not occur when the perturbation wavelength is not relevant to the shear instability. The enhancement of entrainment due to perturbations that excite the small-scale shear instability is consistently observed for  $40 \lesssim Re_\lambda \lesssim 300$ . Similar to the increase in vortices caused by the promoted shear instability, the increase ratio of the entrainment rate remains consistent across this  $Re_\lambda$  range for the same perturbation amplitude normalised by the Kolmogorov velocity. A greater increase in the entrainment rate is observed as the normalised amplitude becomes larger.

This example of entrainment enhancement by exciting small-scale shear instability indicates that this instability has other potential applications in the control and modulation of turbulent flows. One important issue is the enhancement of scalar mixing, which the present study addresses with numerical experiments following Watanabe (2024b). In intermittent turbulent flows involving passive scalar transfer, scalar mixing is strongly influenced by the entrainment process at the TNTI layer. The entrainment locally draws the outer fluid into turbulence, causing an inertial scalar transfer due to fluid motions. Due to the scalar differences between the turbulent and non-turbulent fluids, the entrainment introduces scalar fluctuations within the turbulent flow. Additionally, locally intense scalar gradients appear between the turbulent and non-turbulent regions, contributing to the high dissipation rate of scalar fluctuations (Westerweel *et al.* 2009; Gampert *et al.* 2014; Watanabe *et al.* 2015b, 2016a; Silva & da Silva 2017; Elsinga & da Silva 2019; Kohan & Gaskin 2020). Particularly, scalar dissipation occurs due to small-scale scalar fluctuations, to which small-scale velocity fluctuations induced by the small-scale shear instability can have a significant impact.

The current study explores the potential to enhance passive scalar mixing by inducing instability in small-scale shear layers using weak perturbations. To achieve this, DNSs are conducted on passive scalar mixing within a shear-free turbulent front, characterised as a localised turbulent flow without mean shear that evolves by entraining an outer non-turbulent fluid. This setup represents one of the simplest flows considered in previous studies to investigate intermittent turbulent flows (da Silva & Taveira 2010; Cimarelli *et al.* 2015). This particular flow is chosen for its simplicity; it has no mean shear, which prevents the generation of large-scale coherent structures whose properties strongly depend on flow types, yet it exhibits key features of turbulent mixing in intermittent flows, including entrainment, turbulent scalar transport and molecular diffusion. DNSs are employed to conduct numerical

experiments on the impacts of the sudden introduction of weak velocity perturbations at a single length scale. The perturbation wavelength is selected to excite the instability of small-scale shear layers. The present results reveal that the promoted instability has significant effects on scalar mixing at small scales, including alterations to the geometry of scalar isosurfaces and the statistics of scalar fluctuations.

The paper is organised as follows. Section 2 describes the DNS of the shear-free turbulent front. Section 3 presents the post-processing procedures for the DNS data, which include the conditional statistics for the outer boundary of the scalar mixing layer and the scalar isosurface analysis with an isosurface area density. The results for the perturbation effects on the scalar field are presented in § 4. Finally, the paper is summarised in § 5.

## 2. DNS of a shear-free turbulent front with passive scalar transfer

### 2.1. A shear-free turbulent front with passive scalar transfer

DNS is conducted for a shear-free turbulent front, a setup widely considered in previous studies of turbulence with large-scale intermittency in the absence of mean shear (da Silva & Taveira 2010; Iovieno *et al.* 2014; Cimorelli *et al.* 2015). The numerical details align with those in our previous study on this flow (Watanabe 2024a,b). The initial condition features homogeneous isotropic turbulence (HIT) embedded in a quiescent fluid. The turbulent region expands by entraining the non-turbulent fluid. The cubic computational domain, with dimensions  $L_x \times L_y \times L_z = L^3$ , is discretised into  $N^3$  grid points. The flow evolution is governed by the incompressible Navier–Stokes equations, coupled with the advection–diffusion equation for a passive scalar  $\phi$ , expressed as follows:

$$\frac{\partial u_j}{\partial x_j} = 0, \quad (2.1)$$

$$\frac{\partial u_i}{\partial t} + \frac{\partial u_i u_j}{\partial x_j} = -\frac{1}{\rho} \frac{\partial p}{\partial x_i} + \nu \frac{\partial^2 u_i}{\partial x_j \partial x_j}, \quad (2.2)$$

$$\frac{\partial \phi}{\partial t} + \frac{\partial u_j \phi}{\partial x_j} = D \frac{\partial^2 \phi}{\partial x_j \partial x_j}, \quad (2.3)$$

where  $t$  denotes time,  $x_i$  position,  $u_i$  the velocity vector,  $\rho$  density,  $p$  pressure,  $\nu$  kinematic viscosity,  $\phi$  a passive scalar and  $D$  the diffusivity coefficient for  $\phi$ . The Schmidt number  $Sc = \nu/D$  is assumed to be unity. An in-house finite difference code based on the fractional step method is utilised to solve the governing equations (Watanabe *et al.* 2020; Watanabe & Nagata 2023). Spatial discretisation employs a fourth-order fully conservative central difference scheme (Morinishi *et al.* 1998), while temporal discretisation uses a third-order Runge–Kutta scheme. The BiCGStab method is used to solve the Poisson equation for pressure.

The initial velocity field is generated by modifying the velocity field in HIT,  $\mathbf{u}_{HIT}$ , with a following top-hat function  $C(y)$  as  $C\mathbf{u}_{HIT}$ :

$$C(y) = 0.5 + 0.5 \tanh \left[ \frac{4}{\Delta_I} \left( 1 - \frac{2|y - L/2|}{L_T} \right) \right],$$

where  $C(y) = 1$  corresponds to the turbulent region ( $|y| \lesssim L_T/2$ ) and  $C(y) = 0$  outside it. Here,  $y = 0$  denotes the centre of the flow, and  $(x, z) = (0, 0)$  marks the corner of the  $x$ – $z$  plane. The turbulent front is statistically homogeneous in the  $x$  and  $z$  directions and expands in the  $y$  direction. The periodic boundary conditions are applied in the three directions. The statistics of HIT are evaluated using a spatial average in the computational

domain. Hereafter, the average is denoted by  $\langle f \rangle$  while the fluctuating component of  $f$  is defined as  $f' = f - \langle f \rangle$ . The Kolmogorov length, velocity and time scales are defined as  $\eta = (\nu^3/\langle \varepsilon \rangle)^{1/4}$ ,  $u_\eta = (\nu\langle \varepsilon \rangle)^{1/4}$  and  $\tau_\eta = (\nu/\langle \varepsilon \rangle)^{1/2}$ , respectively, with the kinetic energy dissipation rate  $\varepsilon = 2\nu S_{ij}S_{ij}$  and the rate-of-strain tensor  $S_{ij} = (\partial u_i/\partial x_j + \partial u_j/\partial x_i)/2$ . The statistics evaluated for HIT are indicated with the subscript 0, e.g.  $\eta_0$ . The present DNSs adopt  $L_T = L/3$  and  $\Delta_I = 10\eta_0$ , representing the initial thicknesses of the turbulent front and the interfacial layer, respectively. The scalar distribution of the initial condition is defined by  $\phi = C(y)$ .

The initial field is generated using a DNS database of statistically steady HIT subject to a linear forcing (Carroll & Blanquart 2013). This database has also been employed in our previous studies for investigating the shear layers in HIT (Watanabe *et al.* 2020; Watanabe & Nagata 2023). The HIT was simulated within a triply periodic domain. The present study utilises two DNS databases with the integral-scale based Reynolds number  $Re_{L0} = u_{rms0}L_{I0}/\nu$  set at either 350 or 2200, where the root-mean-squared (rms) value of velocity fluctuations is  $u_{rms} = \sqrt{\langle u'^2 \rangle}$  and the characteristic length at large scales is  $L_I = u_{rms}^3/\langle \varepsilon \rangle$ . Here,  $Re_{L0}$  was evaluated using both time and spatial averages. The size of the computational domain,  $L^3$ , was set as  $L = 5.3L_{I0}$ . The integral time scale of HIT, denoted as  $T_0$ , can be defined as  $T_0 = L_{I0}/u_{rms0}$ .

For  $Re_{L0} = 350$ , five simulations of the shear-free turbulent front are conducted using five independent snapshots of HIT as the initial conditions. In contrast, one simulation is conducted for  $Re_{L0} = 2200$ . The number of small-scale structures increases as the Reynolds number increases. Given that the present study focuses on shear instability at small scales, more simulations are required for a lower  $Re_{L0}$  case to achieve sufficient statistical convergence (Hayashi *et al.* 2021a). The turbulent Reynolds numbers  $Re_\lambda = u_{rms}\lambda/\nu$  evaluated with the snapshots of HIT are  $Re_{\lambda0} = 72$  and 202 for  $Re_{L0} = 350$  and 2200, respectively, where  $\lambda = \sqrt{15\nu u_{rms}^2/\langle \varepsilon \rangle}$  is the Taylor microscale. The ratios between the Taylor microscale and the Kolmogorov scale are  $\lambda/\eta = 17.0$  and 27.9 for  $Re_{L0} = 350$  and 2200, respectively. For these  $Re_{\lambda0}$  values, the shear layer characteristics normalised by Kolmogorov scales are independent of the Reynolds number (Watanabe *et al.* 2020). The number of grid points  $N^3$  are  $512^3$  and  $2024^3$  for  $Re_{L0} = 350$  and 2200, respectively. The spatial resolution  $\Delta = L/N$  is about  $0.8\eta_0$  in the HIT simulations. The same computational parameters are used in the main simulation of the turbulent front, where the velocity field of HIT is modified with  $C(y)$ . Due to the increase in  $\eta$  over time as the turbulence decays,  $\Delta/\eta$  continuously decreases during the simulation of the turbulent front. Figure 1 visualises the growth of the turbulent front with two-dimensional profiles of  $\phi$ . The present study defines the region  $0 < \phi < 1$  as a scalar mixing layer, which spatially develops over time. Initially, two scalar mixing layers are present on both sides of the turbulent region, and each scalar mixing layer spreads both outward and inward relative to the turbulent front. Consequently, the centre of the turbulent front ( $y = 0$ ) is influenced by both scalar mixing layers.

## 2.2. Perturbations introduced in the shear-free turbulent front

This study investigates the effects of velocity perturbations introduced into the turbulent front on passive scalar mixing, with a focus on perturbations whose wavelength corresponds to the unstable mode of small-scale shear layers. Drawing on insights from an earlier study of the perturbation effects in decaying HIT (Watanabe & Nagata 2023), solenoidal perturbations are superimposed on the velocity field after the flow evolves over  $0.5T_0$ . By this time, the influence of the initialisation with the artificial interface has disappeared, as confirmed by velocity gradient statistics near the TNTI layer. Figure 2 presents the normalised longitudinal energy spectra of  $u$  at the centre of the turbulent front, calculated at  $t = 0.5T_0$

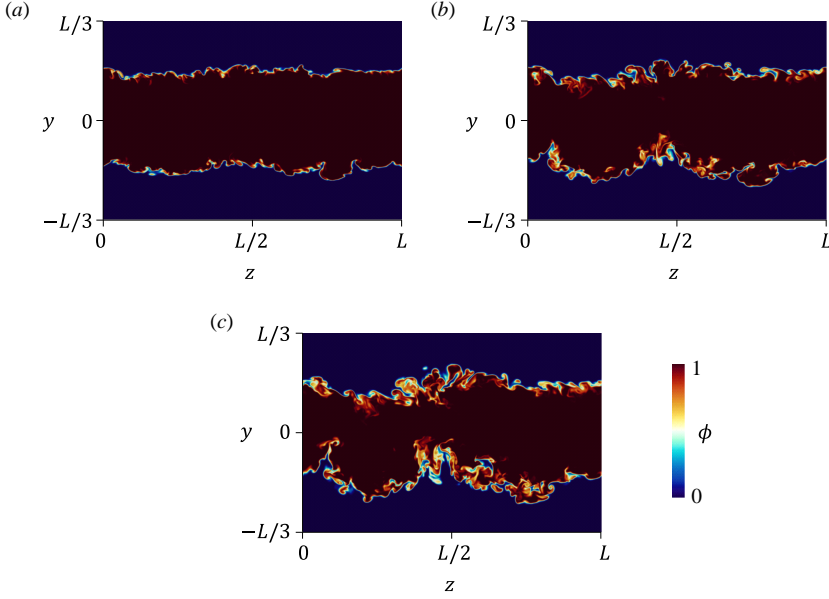


Figure 1: Temporal evolution of the shear-free turbulent front visualised by passive scalar  $\phi$ : (a)  $t = 7\tau_{\eta 0}$ , (b)  $t = 14\tau_{\eta 0}$  and (c)  $t = 21\tau_{\eta 0}$  in R2200.

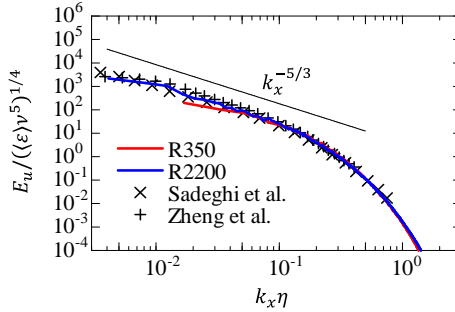


Figure 2: Normalised longitudinal energy spectra of  $u$ ,  $E_u(k_x)$ , at the centre of the turbulent front ( $y = 0$ ) at the moment of perturbation introduction. The spectra are evaluated without perturbations. The present DNS results are compared with experiments of a turbulent round jet at  $Re_\lambda \approx 170$  (Sadeghi *et al.* 2014) and active-grid turbulence at  $Re_\lambda \approx 240$  (Zheng *et al.* 2021). The spectra  $E_u$  and the wavenumber in the  $x$ -direction,  $k_x$ , are normalised by the mean kinetic energy dissipation rate  $\langle \epsilon \rangle$ , kinematic viscosity  $\nu$  and Kolmogorov scale  $\eta$ .

before the introduction of perturbations, for  $Re_{L0} = 350$  and 2200. For the low  $Re_{L0}$  case, the scale separation between large and small scales is insufficient to observe the  $k_x^{-5/3}$  law. This power law is observed for  $Re_{L0} = 2200$ . The DNS results for  $Re_{L0} = 2200$  generally agree with experimental data from a round jet (Sadeghi *et al.* 2014) and active-grid turbulence (Zheng *et al.* 2021).

Three cases are tested for the perturbation location: within the turbulent front, outside the turbulent front, and across the entire flow region. The perturbations are represented by



sinusoidal functions as follows:

$$\mathbf{u}_P = \left[ u_f \sin\left(\frac{2\pi y}{\lambda_f}\right), u_f \sin\left(\frac{2\pi z}{\lambda_f}\right), u_f \sin\left(\frac{2\pi x}{\lambda_f}\right) \right],$$

which satisfies a divergence-free condition. The wavelength  $\lambda_f$  and the amplitude  $u_f$  are the perturbation parameters. The turbulent region can be identified by the vorticity magnitude  $\omega = |\nabla \times \mathbf{u}|$  (Bisset *et al.* 2002). With the mean vorticity magnitude  $\langle \omega \rangle$  at the centre,  $y = 0$ , the turbulent and non-turbulent regions are defined as  $\omega/\langle \omega \rangle \geq \omega_{th}$  and  $\omega/\langle \omega \rangle < \omega_{th}$ , respectively. An appropriate value for the threshold  $\omega_{th}$  is within the range where the detected turbulent volume remains unchanged with a variation of  $\omega_{th}$  (Taveira *et al.* 2013). Based on this criterion,  $\omega_{th} = 0.01$  is used to identify the turbulent front. Appendix A details the method used to determine  $\omega_{th}$ . The detection function is defined as  $X_\omega = 0$  and 1 in the turbulent and non-turbulent regions, respectively. External perturbations are defined as  $X_\omega \mathbf{u}_P$ , while internal ones are  $(1 - X_\omega) \mathbf{u}_P$ . These velocity perturbations are superimposed on the velocity field of the turbulent front. When the perturbation is introduced throughout the entire flow region,  $\mathbf{u}_P$  is added uniformly to the velocity field across the entire domain. A similar approach was also adopted in DNS of a temporally developing turbulent boundary layer subject to freestream turbulence (Kozul *et al.* 2020). Perturbation parameters  $\lambda_f$  and  $u_f$  are set according to the Kolmogorov scales. The scale evaluation is based on the volume average in the turbulent region, defined as  $\langle f \rangle_V = V_\omega^{-1} \iiint_V (1 - X_\omega) f dx dy dz$  with the volume integral in the computational domain, where  $V_\omega$  is the turbulent volume. The Kolmogorov length, time and velocity scales calculated with the volume-averaged energy dissipation rate inside the turbulent region at the time of perturbation introduction are denoted by  $\eta_P$ ,  $\tau_{\eta P}$  and  $u_{\eta P}$ , respectively. These scales are used to determine the computational parameters as described below.

The present study employs numerical simulations to implement idealised perturbation conditions, such as maintaining a consistent normalised amplitude across different Reynolds numbers, to explore the effects of perturbations at the unstable wavelength of shear layers. This approach allows for precise control over experimental variables, which can be challenging to achieve in laboratory experiments. However, in laboratory settings, various methods are available for introducing these perturbations. Placing an object with a specific target length scale in a mean flow can induce velocity fluctuations, as demonstrated by spectral analyses of various wakes in previous studies (Britter *et al.* 1979; Nagata *et al.* 2020b; Kato *et al.* 2022). Another method involves using fluidic actuators, which can adjust their actuation frequency or spatial arrangement to generate flow disturbances at a specific length scale (Cattafesta III & Sheplak 2011).

### 2.3. Computational parameters

The main computational and physical parameters are summarised in table 1. The simulations of turbulent fronts without any perturbations are designated as  $Ra$ , where  $a$  represents the Reynolds number, with  $a = 350$  and  $2200$  denoting  $Re_{L0} = 350$  and  $2200$ , respectively. Cases incorporating perturbations are designated as  $RaLbn$ , where  $b$  specifies the perturbation wavelength  $\lambda_f$  as  $\lambda_f = b\eta_P$ , and  $n = e, i$  or  $ei$  indicates the perturbation location. Perturbations are introduced outside the turbulent front for  $n = e$  (external perturbations), inside the turbulent front for  $n = i$  (internal perturbations), and throughout the entire domain for  $n = ei$ . Perturbations with  $b \approx 30$  possess the wavelength close to the unstable mode of small-scale shear layers. The wavelength dependence is thoroughly examined for  $Re_{L0} = 350$  with external perturbations with  $\lambda_f$  between  $8\eta_P$  and  $210\eta_P$ . For  $Re_{L0} = 2200$ , two cases, R2200 and R2200L30e, are simulated. Additionally, perturbations inside the turbulent front or in the entire flow region with  $\lambda_f = 30\eta_P$  are tested for  $Re_{L0} = 350$ , denoted as R350L30i



Table 1: Computational parameters of DNS.

Run	$Re_{L0}$	$Re_\lambda$	Perturbation types	$u_f/u_{\eta P}$	$\lambda_f/\eta_P$	$k_P/k_T$	$\Delta/\eta$
R350	350	55–72	Without perturbation	0	–	0	0.55–0.82
R350L8e	350	55–72	External perturbation	1.4	8	6.0%	0.55–0.82
R350L12e	350	55–72	External perturbation	1.4	12	6.0%	0.55–0.82
R350L16e	350	55–72	External perturbation	1.4	16	6.0%	0.55–0.82
R350L20e	350	55–72	External perturbation	1.4	20	6.0%	0.55–0.82
R350L24e	350	55–72	External perturbation	1.4	24	6.0%	0.55–0.82
R350L28e	350	55–72	External perturbation	1.4	28	6.0%	0.55–0.82
R350L30e	350	55–72	External perturbation	1.4	30	6.0%	0.55–0.82
R350L32e	350	55–72	External perturbation	1.4	32	6.0%	0.55–0.82
R350L36e	350	55–72	External perturbation	1.4	36	6.0%	0.55–0.82
R350L40e	350	55–72	External perturbation	1.4	40	6.0%	0.55–0.82
R350L44e	350	55–72	External perturbation	1.4	44	6.0%	0.55–0.82
R350L52e	350	55–72	External perturbation	1.4	52	6.0%	0.55–0.82
R350L68e	350	55–72	External perturbation	1.4	68	6.0%	0.55–0.82
R350L84e	350	55–72	External perturbation	1.4	84	6.0%	0.55–0.82
R350L116e	350	55–72	External perturbation	1.4	116	6.0%	0.55–0.82
R350L210e	350	55–72	External perturbation	1.4	210	6.0%	0.55–0.82
R350L30i	350	53–72	Internal perturbation	1.4	30	6.0%	0.56–0.82
R350L30ei	350	53–72	Perturbation in an entire flow region	1.4	30	6.0%	0.56–0.82
R2200	2200	131–202	Without perturbation	0	–	0	0.68–0.82
R2200L30e	2200	131–202	External perturbation	1.4	30	2.5%	0.68–0.82

and R350L30ei, respectively. An example of external perturbations is shown in figure 3(a), which visualises the enstrophy field in R2200L30e. The passive scalar at the same visualised plane is shown in figure 3(b). The present study delves into how these perturbations affect passive scalar mixing.

The present study focuses on the instability of small-scale shear layers. The instability wavelength of shear layers is determined by their thickness, which is proportional to the Kolmogorov scale (Corcos & Lin 1984; Watanabe & Nagata 2023). In addition, the mean velocity jump across the shear layers is also proportional to the Kolmogorov velocity (Watanabe *et al.* 2020). These velocity and thickness scales indicate that the time scale of shear layer evolution is determined by the Kolmogorov time scale, as confirmed by the observed process of vortex formation due to small-scale shear instability (Watanabe *et al.* 2020). Therefore, the perturbation parameters and simulation time are chosen based on the Kolmogorov scales. All perturbations have the same amplitude of  $u_f = 1.4u_{\eta P}$ . In all simulations, the perturbations are imposed at  $t = 0.5T_0$ , and then the flow evolution is simulated over  $15\tau_{\eta P}$  until  $t = 0.5T_0 + 15\tau_{\eta P}$ . Time after introducing perturbations is denoted by  $\tau = t - 0.5T_0$ . Table 1 includes the turbulent Reynolds number  $Re_\lambda$  and spatial resolution  $\Delta/\eta$  at the flow centre,  $y = 0$ , at  $t = 0$  and  $0.5T_0 + 15\tau_{\eta P}$ . For the sinusoidal velocity perturbations, the kinetic energy per unit mass added by the perturbations,  $k_P$ , depends on  $u_f$  but is independent of  $\lambda_f$ . The table also presents  $k_P$  normalised by the turbulent kinetic energy  $k_T = \langle u'^2 + v'^2 + w'^2 \rangle / 2$  at the centre of the turbulent front at the time of perturbation introduction. Under the present conditions, values of  $k_P/k_T$  are 6.0% for  $Re_{L0} = 350$  cases and 2.5% for  $Re_{L0} = 2200$  cases, indicating that the perturbations are weaker than the turbulent velocity fluctuations. Since the normalised Kolmogorov velocity

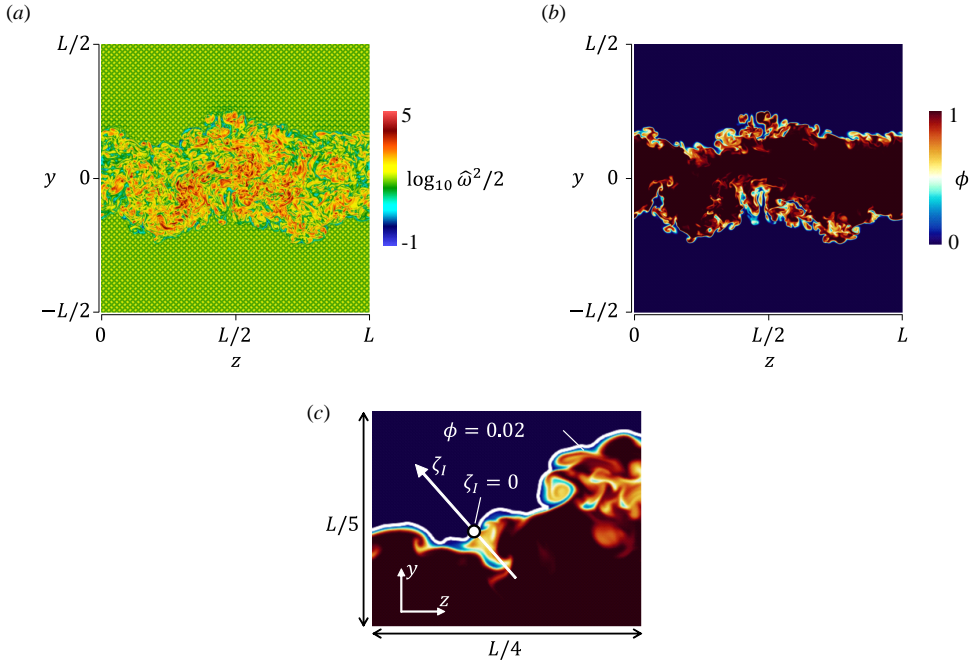


Figure 3: Two-dimensional profiles of (a) enstrophy  $\omega^2/2$  and (b) passive scalar  $\phi$  at  $\tau/\tau_{\eta P} = 1.1$  in R2200L30e, where enstrophy is normalised by  $L_0$  and  $u_{rms0}$  such that  $\hat{\omega}^2/2 = (\omega^2/2)/(u_{rms0}^2/L_0^2)$ . (c) Local coordinate  $\zeta_I$  defined for detailed analysis near the outer boundary of the scalar mixing layer.

353  $u_{\eta P}/\sqrt{k_T}$  decreases with the Reynolds number,  $k_P/k_T$  with a fixed value of  $u_f/u_{\eta P} = 1.4$   
 354 becomes smaller as the Reynolds number increases.

355 More thorough investigations into the dependencies on Reynolds number and perturbation  
 356 parameters were conducted in Watanabe & Nagata (2023) and Watanabe (2024a). These  
 357 studies focused on the increased number of vortex tubes and concomitant changes in turbulent  
 358 characteristics, such as the energy dissipation rate and entrainment rate defined by enstrophy  
 359 transport, which occur when the perturbation wavelength matches the unstable mode of small-  
 360 scale shear layers. DNS within the range of  $40 \lesssim Re_\lambda \lesssim 300$  in these studies demonstrated  
 361 that the effects of perturbations with  $\lambda_f/\eta_P \approx 30$  are unaffected by the Reynolds number,  
 362 provided that  $u_f/u_{\eta P}$  is identical. Furthermore, the degree of turbulence modulation is well  
 363 characterised by  $u_f/u_{\eta P}$  rather than  $u_f$  normalised by the root-mean-square of velocity  
 364 fluctuations, i.e. the velocity scale at large scales. An increase in  $u_f/u_{\eta P}$  results in more  
 365 pronounced effects on the small-scale shear layers. For this reason, the present study conducts  
 366 all DNS for  $u_f/u_{\eta P} = 1.4$ , and any increase or decrease in  $u_f/u_{\eta P}$  would result in stronger and  
 367 weaker but qualitatively similar effects of perturbation. Another type of perturbation, such  
 368 as random velocity fluctuations generated with an inverse fast Fourier transform by adapting  
 369 random phases and a predetermined energy spectrum, also yielded almost identical results  
 370 to sinusoidal perturbations with a constant phase. The time scale of the shear instability  
 371 promoted by perturbations is also determined by the Kolmogorov time scale. Therefore,  
 372 the simulation duration in this study is determined by  $\tau_{\eta P}$ . These previous studies provide  
 373 supplemental information to the present DNS, which focuses on the perturbation effects on  
 374 passive scalar mixing.

375 The turbulent front subject to external perturbations relates closely to studies of the

interface between two different turbulent regions, known as a turbulent/turbulent interface (TTI) layer. A similar layer forms between the turbulent front and external perturbations, although the perturbations do not have turbulence properties. Recent studies have demonstrated that the interface geometry and entrainment rate of primary turbulence are altered by the effects of background turbulence (Kankanwadi & Buxton 2020; Kohan & Gaskin 2022; Chen & Buxton 2023; Huang *et al.* 2023). These studies mostly focus on large-scale background turbulence with an integral scale similar to that of primary turbulence. The TTI layer forms along shear layers (Nakamura *et al.* 2023). Background turbulence can influence this layer in ways similar to the external perturbations considered in this study. Although sinusoidal perturbations lack the multi-scale nature of background turbulence, the insights from this study on the effects of small-scale shear instability are valuable for understanding how small-scale velocity fluctuations in background turbulence influence the TTI layer. Related studies investigate turbulent boundary layers developing in freestream turbulence (Hancock & Bradshaw 1989; Sharp *et al.* 2009; Nagata *et al.* 2011; Dogan *et al.* 2016; Wu *et al.* 2019; Kozul *et al.* 2020; Jooss *et al.* 2021). These studies typically evaluate the length of freestream turbulence in terms of boundary layer thickness, whereas the primary parameter in the present study is the length scale ratio between the perturbation scale and the Kolmogorov scale. For this reason, direct comparisons of the present DNS with these previous studies are not feasible. However, the effects of small-scale freestream turbulence on the fully-developed turbulent boundary layer may be relevant to the present simulations involving small-scale perturbations.

Shear layers have also been identified between uniform momentum zones in wall-bounded shear flows (Eisma *et al.* 2015; Fan *et al.* 2019; Gul *et al.* 2020; Chen *et al.* 2021; Kwon *et al.* 2014). These shear layers exhibit a thickness close to the Taylor microscale and may differ from the small-scale shear layers examined in this study. However, as these shear layers separate distinct flow regions with differing characteristics, turbulent motions near the shear layers may influence their instability, similar to the perturbation effects observed on shear layers in the present DNS.

### 3. Analyses of the passive scalar field in the turbulent front

#### 3.1. Conditional statistics

The effects of perturbations that promote small-scale shear instability are examined for the scalar mixing layer, which is characterised by the scalar field (Bilger *et al.* 1991; Iovieno *et al.* 2014). This layer exhibits external intermittency similar to jets and wakes: both external and internal fluids of the scalar mixing layer are observed at a fixed  $y$  position, as visibly shown in figure 3(b). Spatial averages taken on  $x$ - $z$  planes,  $\langle f \rangle$ , define conventional statistical quantities, which may not accurately reflect the properties of the scalar mixing layer because they include areas outside it as statistical samples. The external perturbations considered in this study influence the mixing process through the outer interfacial layer that appears on the low- $\phi$  side. This layer resembles the TNTI layer, whose properties have been investigated using conditional statistics calculated as functions of the distance from the vorticity isosurface bounded by non-turbulent fluids (Bisset *et al.* 2002). The present study adopts a similar methodology to explore the progress of mixing in the scalar mixing layer. The outer boundary of the scalar mixing layer is defined as a scalar isosurface at  $\phi = \phi_{th}$  (Bilger *et al.* 1976; Chen & Blackwelder 1978; Murlis *et al.* 1982; Kim & Bilger 2007). This threshold-based approach has successfully identified the boundaries of the scalar mixing layers in other flow configurations (Blakeley *et al.* 2023; Nakamura *et al.* 2023). In all simulations, the present study adopts  $\phi_{th} = 0.02$ . This threshold is determined using the same methodology as  $\omega_{th}$

for detecting the turbulent front. Appendix A provides details on how  $\phi_{th} = 0.02$  is chosen and examines the  $\phi_{th}$  dependence of the main results presented in this paper.

Conditional statistics are evaluated as functions of the distance from the scalar isosurface of  $\phi = \phi_{th}$ . At each point on this scalar isosurface, a local coordinate  $\zeta_I$  is introduced, aligned with the direction normal to the surface,  $\mathbf{n} = -\nabla\phi/|\nabla\phi|$ . In this setup,  $\zeta_I > 0$  and  $\zeta_I < 0$  correspond to regions outside and inside the scalar mixing layer, respectively. This local coordinate is discretised with a constant spacing of  $0.5\eta$ , where  $\eta$  is evaluated at the centre of the turbulent front. The range examined for  $\zeta_I$  spans from  $-50 \leq \zeta_I/\eta \leq 50$ . Variables defined on the DNS grids are interpolated onto the discretised points of  $\zeta_I$  using tri-linear interpolation. This interpolation process is repeated for all local coordinates defined at different positions on the scalar isosurface. Subsequently, ensemble averages are evaluated as functions of  $\zeta_I$ . This average is denoted by  $\langle f \rangle_I$ . Importantly, regions with  $\phi > \phi_{th}$  and  $\phi < \phi_{th}$  are excluded from the averaging procedures for  $\zeta_I > 0$  and  $\zeta_I < 0$ , respectively, ensuring that the statistics are calculated solely for the inside or outside of the scalar mixing layer. This methodology mirrors the approach used in evaluating the conditional statistics near the TNTI layer, and further details can be found in Watanabe *et al.* (2018).

### 3.2. Analysis of scalar isosurface

The behaviour of the scalar isosurface is crucial in the development of the scalar mixing layer. This surface is analysed using the isosurface area density  $\Sigma'$  following the scalar isosurface analysis methodologies employed in mixing layers (Blakeley *et al.* 2022, 2023). The description of the isosurface area density provided herein aligns with these original papers, which should be referred to for further details. Here, the outer boundary of the scalar mixing layer is analysed with the isosurface area density of the scalar isosurface  $\phi = \phi_{th}$ . An indicator function,  $X_\phi(x, y, z)$ , is introduced with the following definition:

$$X_\phi(x, y, z) = \begin{cases} 1 & \text{for } (\phi(x, y, z) \leq \phi_{th}) \\ 0 & \text{for } (\phi(x, y, z) > \phi_{th}) \end{cases}. \quad (3.1)$$

The isosurface area density, expressed as  $\Sigma' = |\nabla\phi|\delta(\phi - \phi_{th})$  with the delta function, is defined such that its volume integral over the computational domain  $\mathcal{V}$  yields the isosurface area  $A$ , as  $A = \iiint_{\mathcal{V}} \Sigma' dx dy dz$  (Pope 1988). Equation (3.1) can be reformulated using the Heaviside function  $H$  as  $X[\phi(x, y, z)] = H[-(\phi - \phi_{th})]$ . From this, the following expression for the isosurface area density is derived by utilising the relationship between the delta and Heaviside functions:

$$\Sigma'(x, y, z) = -\frac{1}{\sqrt{(\partial\phi/\partial x_i)^2}} \frac{\partial X_\phi}{\partial x_j} \frac{\partial \phi}{\partial x_j}. \quad (3.2)$$

For any function  $f$ , its surface integral, denoted as  $[f]_S$ , is expressed with a volume integral,  $[f]_S = \iiint_{\mathcal{V}} f \Sigma' dx dy dz$ , while the surface average,  $\langle f \rangle_S$ , is written as  $\langle f \rangle_S = [f]_S/A$ .

The evolution of the scalar mixing layer is intricately linked to the propagation of the scalar isosurface, influenced by the diffusive effects on  $\phi$ . This study specifically focuses on the low- $\phi$  side, namely the isosurface of  $\phi = \phi_{th}$ , where external perturbations significantly affect the mixing process. A scalar isosurface at a point  $(x, y, z)$  propagates with a speed of  $v_P = |\nabla\phi|^{-1} D \nabla^2 \phi$  in the direction represented by  $\mathbf{n} = -\nabla\phi/|\nabla\phi|$ . The volume of fluid enclosed by the scalar isosurface is calculated by integrating  $1 - X_\phi$  over the domain, denoted as  $V_S = \iiint_{\mathcal{V}} (1 - X_\phi) dx dy dz$ . The growth rate of this volume,  $\dot{V}_S = dV_S/dt$ , is expressed through the isosurface integral of  $v_P$  as  $\dot{V}_S = [v_P]_S$ . This metric quantifies the amount of fluid drawn into the scalar mixing layer due to molecular diffusion on the low- $\phi$  side. Here, positive  $\dot{V}_S$  values indicate an expansion of the scalar mixing layer. The mean propagation

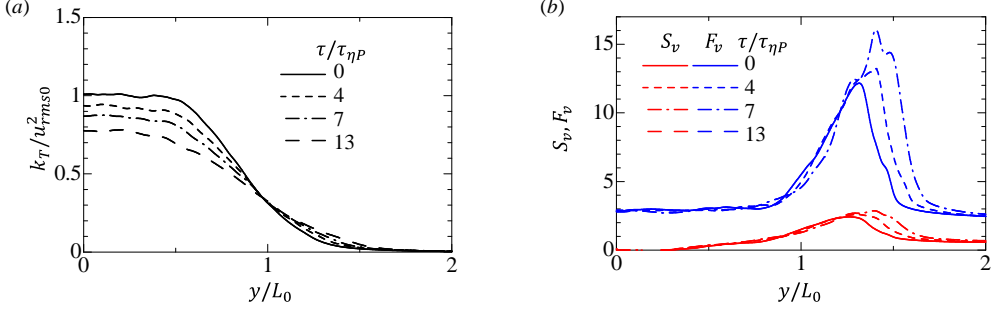


Figure 4: Lateral profiles of (a) turbulent kinetic energy  $k_T$  and (b) skewness and flatness of lateral velocity, respectively denoted by  $S_v$  and  $F_v$ , in R2200.

velocity is then defined as  $V_P = [v_P]_S / A$ . These metrics are employed to assess the effects of perturbations on the growth of the scalar mixing layer.

The growth of the scalar mixing layer is critically influenced by the area of the scalar isosurface,  $A$ . The temporal evolution of  $A$  normalised by the surface area of an  $x$ - $z$  plane of the computational domain,  $A' = A / L_x L_z$ , is related to the governing equation of the mean isosurface area density  $\Sigma(y, t) = \langle \Sigma' \rangle$ , which is expressed as follows:

$$\frac{\partial \Sigma}{\partial t} + \frac{\partial \langle u_i \rangle_S \Sigma}{\partial x_i} = - \left\langle n_i n_j \frac{\partial u_i}{\partial x_j} \right\rangle_S \Sigma - \frac{\partial}{\partial x_i} \left( \langle v_P n_i \rangle_S \Sigma \right) + \left\langle v_P \frac{\partial n_i}{\partial x_i} \right\rangle_S \Sigma. \quad (3.3)$$

The normalised surface area,  $A'(t)$ , is also expressed as  $A'(t) = \int_{-L_y/2}^{L_y/2} \Sigma dy$ . For the current flow configuration, which exhibits statistical homogeneity in the  $x$  and  $z$  directions, the governing equation for  $A'$  is derived by integrating the above equation as:

$$\frac{\partial A'}{\partial t} = - \int_{-L_y/2}^{L_y/2} \left\langle n_i n_j \frac{\partial u_i}{\partial x_j} \right\rangle_S \Sigma dy + \int_{-L_y/2}^{L_y/2} \left\langle v_P \frac{\partial n_i}{\partial x_i} \right\rangle_S \Sigma dy = P_A + D_A. \quad (3.4)$$

Here,  $P_A$  represents the surface deformation due to the local velocity gradient, effectively capturing the mechanical effects of the turbulence on the isosurface. The second term  $D_A$  denotes the impact of isosurface propagation caused by molecular diffusion. The decomposition of the velocity gradient tensor into the rate-of-strain tensor  $S_{ij} = (\partial u_i / \partial x_j + \partial u_j / \partial x_i) / 2$  and the rate-of-rotation tensor  $\Omega_{ij} = (\partial u_i / \partial x_j - \partial u_j / \partial x_i) / 2$  yields  $n_i n_j (\partial u_i / \partial x_j) = n_i n_j S_{ij} + n_i n_j \Omega_{ij}$ , where  $P_A$  is expressed in terms of these components. Since  $\Omega_{ij}$  is an anti-symmetric tensor, it follows that  $n_i n_j \Omega_{ij} = 0$ . Thus,  $P_A$  represents the change in the isosurface area due to the fluid deformation characterised by  $S_{ij}$ .

## 4. Results and discussion

### 4.1. The development of the turbulent front and perturbations

The fundamental properties of the shear-less turbulent front are examined through the lateral profiles of velocity statistics, with results presented for  $y \geq 0$  due to statistical symmetry at  $y = 0$ . Figure 4(a) showcases the lateral profiles of turbulent kinetic energy  $k_T = \langle u'^2 + v'^2 + w'^2 \rangle / 2$  in R2200. In the central region,  $k_T$  exhibits a uniform distribution and decays over time. For  $y/L_0 > 1$ ,  $k_T$  increases with time owing to the spatial development of the turbulent front, which reduces the uniform  $k_T$  region.

Figure 4(b) illustrates the skewness and flatness of the lateral velocity component, defined as  $S_v = \langle v'^3 \rangle / v_{rms}^3$  and  $F_v = \langle v'^4 \rangle / v_{rms}^4$ , respectively. For reference, the skewness and

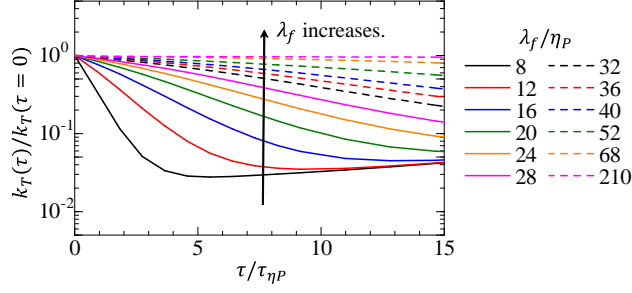


Figure 5: Temporal variations of turbulent kinetic energy in the perturbation region,  $k_T(\tau)$ , normalised by its initial value,  $k_T(\tau = 0)$ . Results from the R350 series with external perturbations are compared for different wavelengths  $\lambda_f/\eta_P$ .

500 flatness values of a Gaussian probability distribution are  $S_v = 0$  and  $F_v = 3$ , respectively.  
 501 In the central region, the values are approximately  $S_v \approx 0$  and  $F_v \approx 3$ . When two turbulent  
 502 flows with different scales interact, such as in a shear-less turbulent mixing layer formed  
 503 between different grid turbulence generated by two grids, the intermittency of large-scale  
 504 motions can lead to increases in  $S_v$  and  $F_v$  (Veeravalli & Warhaft 1989; Kang & Meneveau  
 505 2008; Matsushima *et al.* 2021; Nakamura *et al.* 2022). These studies have shown that large-  
 506 scale motions from a high turbulent kinetic energy region intermittently penetrate into a  
 507 low turbulent kinetic energy region. The current results with one side remaining irrotational  
 508 also highlight increases in  $S_v$  and  $F_v$  with peaks occurring between  $1.3 < y/L_0 < 1.4$ . The  
 509 development of the flow causes an outward shift in the locations of these peaks. The present  
 510 DNS, initiated by inserting HIT into quiescent fluid, effectively reproduces the large-scale  
 511 intermittency characteristic of this flow. Here,  $S_v > 0$  is associated with large-scale turbulent  
 512 motions penetrating into the non-turbulent region, where velocity fluctuations are primarily  
 513 governed by irrotational motion induced by turbulence (da Silva & Pereira 2008). Even in  
 514 the non-turbulent region at  $y/L_0 \approx 2$ ,  $S_v$  maintains a small but non-zero value, indicating  
 515 the influence of intermittent turbulent motion that causes  $S_v > 0$ .

516 The perturbations introduced at a given time instance subsequently decay over time.  
 517 Figure 5 illustrates the decay of perturbations by plotting the turbulent kinetic energy of  
 518 external perturbations as a function of time. The R350 series is compared for different  
 519 wavelength values. Here, the turbulent kinetic energy  $k_T$  is evaluated by calculating the  
 520 spatial average of  $(u^2 + v^2 + w^2)/2$  over  $|y/L_0| > 2.0$ , which is always outside the turbulent  
 521 front. Small-scale perturbations tend to decay rapidly with time. For  $\lambda_f/\eta_P = 8$ –16,  $k_T$   
 522 reaches a minimum value and then begins to increase, driven by velocity fluctuations from  
 523 large-scale motions induced by the turbulent front. Thus, the direct effects of small-scale  
 524 perturbations are significant only at early times. As the wavelength increases, the decay of  
 525 perturbation energy slows, allowing the external perturbations to continuously influence flow  
 526 evolution.

#### 527 4.2. External perturbation effects on the outer boundary of scalar mixing layer

528 The effects of external perturbations on the outer boundary of the scalar mixing layer,  
 529 delineated by the scalar isosurface, are examined herein. Previous DNS studies indicate  
 530 that small-scale shear layers predominantly manifest within the TNTI layer, forming at  
 531 the outer boundary of the turbulent front (Hayashi *et al.* 2021b). The external perturbations,  
 532 particularly those with the unstable wavelength of small-scale shear instability, are anticipated  
 533 to significantly influence the evolution of shear layers near this boundary. Figure 6 visualises  
 534 the evolution of shear layers near the boundary, viewed from the direction of  $y > 0$ . The triple





Figure 6: Temporal evolutions of small-scale shear layers and vortex tubes at different time instances ( $\tau/\tau_{\eta P} = 1.3, 3.7, 5.5$  and  $7.3$ ) progressing from left to right in each panel: (a) R350, (b) R350L30e and (c) R350L210e. The shear layers (grey) and vortex tubes (orange) are visualised respectively by the isosurfaces of shear intensity  $I_S = 1.5\langle I_S \rangle$  and rigid-body-rotation intensity  $I_R = 3\langle I_R \rangle$ , with averages used as reference values taken at the flow centre. The visualised domain is a cube of size  $L_0^3$ , with the walls coloured by  $I_S$ .

decomposition of the velocity gradient tensor is employed to quantify the intensities of shear and rigid-body rotation, denoted by  $I_S$  and  $I_R$  respectively (Hayashi *et al.* 2021a). The shear layers and vortex tubes are identified using  $I_S$  and  $I_R$ , respectively. While the perturbations contribute to vorticity outside the scalar mixing layer, they are too weak to be recognised as shear layers or vortex tubes. When no perturbations are added in R350, as shown in figure 6(a), the shear layer labeled as ‘S’ evolves over time without producing any vortex tubes. In contrast, the introduction of a perturbation with the unstable wavelength in R350L30e leads to the formation of a vortex tube, labeled as ‘V’ in figure 6(b). This promotion of vortex formation is absent in R350L210e, which uses a larger perturbation wavelength, as visualised in figure 6(c). Similarly, no vortex formation is promoted in R350L8e (not shown here), which employs a much smaller wavelength than the unstable one. External perturbations introduced outside the turbulent front prove effective in exciting small-scale shear instability near the boundary only when the wavelength approximates 30 times the Kolmogorov scale, which aligns with the unstable mode of the shear layers. This finding is consistent with numerical experiments involving internal perturbations (Watanabe & Nagata 2023; Watanabe 2024a), where artificial velocity perturbations of about 30 times the Kolmogorov scale, when superimposed inside turbulence, cause many small-scale shear layers to become unstable and produce vortex tubes.

Figure 7(a) displays the temporal variation of the surface-integrated propagation velocity of the scalar isosurface,  $\dot{V}_S = [\dot{V}_P]_S$ , which represents the growth rate of the scalar mixing layer contributed from the low-scalar-value sides. Here, the integral is taken for the scalar isosurfaces on both flow sides. The effects of perturbations are compared across



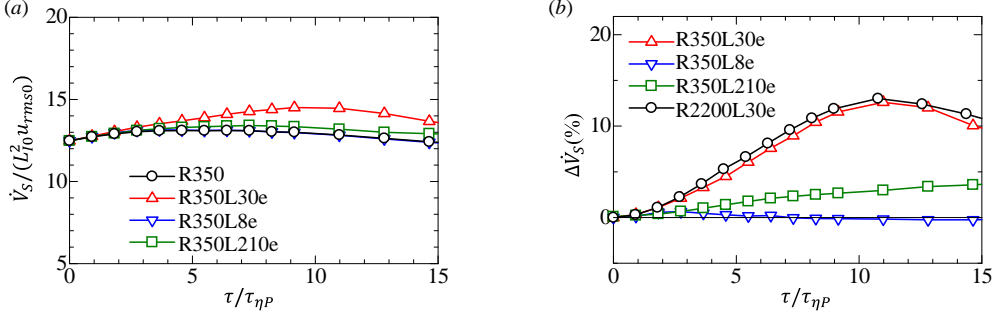


Figure 7: (a) Growth rate  $\dot{V}_S$  of the scalar mixing layer contributed from the low-scalar side in the series of R350. (b) Increase ratio in  $\dot{V}_S$  due to external perturbations, denoted as  $\Delta \dot{V}_S$ .

the R350 series. The growth rate is significantly enhanced by perturbations with the unstable wavelength of shear layers in R350L30e compared to the baseline case R350. A subtle increase is observed for R350L210e with a larger wavelength, while the growth rate remains largely unaffected in the case of a smaller wavelength. All cases adopt the same perturbation amplitude, illustrating that perturbations efficiently increase the growth rate when the wavelength matches the unstable mode of small-scale shear layers. Figure 7(b) shows the relative change in  $\dot{V}_S$ , denoted as  $\Delta \dot{V}_S$ . Throughout the paper,  $\Delta f$  is defined as  $(f_1 - f_2)/f_2$ , where  $f_1$  and  $f_2$  are statistical quantities in simulations with and without perturbations, respectively. The perturbation effect becomes increasingly pronounced in  $\dot{V}_S$  with time, with increments due to perturbations exceeding 10% from the baseline cases in R350L30e and R2200L30e. The increases in  $\dot{V}_S$  in R350L30e and R2200L30e are almost identical despite differing Reynolds numbers. These two cases with the unstable wavelength of shear layers adopt the same normalised perturbation amplitude  $u_f/u_{\eta P} = 1.4$ , and the perturbation in R2200L30e with smaller  $u_{\eta P}$  has less kinetic energy than that in R350L30e. Therefore, even a weaker perturbation can lead to the same enhancement effect on the growth rate of the scalar mixing layer at a higher Reynolds number. The peak in  $\Delta \dot{V}_S$  is attained at  $\tau/\tau_{\eta P} \approx 11$  in both R350L30e and R2200L30e, suggesting that the time scale for enhancing the scalar mixing layer growth is related to the Kolmogorov time scale. This temporal evolution aligns with the visualisation of the unstabilised shear layer in figure 6(b), where vortex formation due to the perturbation occurs over a span of about  $10\tau_{\eta P}$ . These scalings based on  $u_{\eta P}$  and  $\tau_{\eta P}$  relate to the scaling of small-scale shear layers, whose characteristic velocity and length scales are  $u_\eta$  and  $\eta$ , respectively (Watanabe *et al.* 2020; Fiscaletti *et al.* 2021).

The growth rate  $\dot{V}_S$  is expressed as  $\dot{V}_S = AV_P$ , where  $A$  is the isosurface area and  $V_P$  is the mean propagation velocity. Figure 8(a) illustrates the relative change in  $A$  due to perturbations, denoted as  $\Delta A$ . The temporal variation of  $\Delta A$  closely mirrors that of  $\Delta \dot{V}_S$ , with the surface area also increasing by more than 10%, comparable to the peak in  $\Delta \dot{V}_S$ , when the perturbations feature the unstable wavelength of small-scale shear layers. Thus, the increase in  $\dot{V}_S$  is predominantly driven by the perturbation effect on  $A$ , although  $V_P$  also experiences a slight increase due to the perturbation (the increase is less than 1.5% and is not shown in the figure). Consequently, the rapid growth of the scalar mixing layer in cases R350L30e and R2200L30e is attributed to the enlarged area of the outer boundary of the scalar mixing layer, facilitating efficient scalar transfer from the inside to the outside, thereby expanding the scalar mixing layer.

The increases in the growth rate,  $\Delta \dot{V}_S$ , and the surface area,  $\Delta A$ , are similar for R350L30e and R2200L30e, both of which use the same normalised perturbation parameters,  $\lambda_f/\eta_P =$

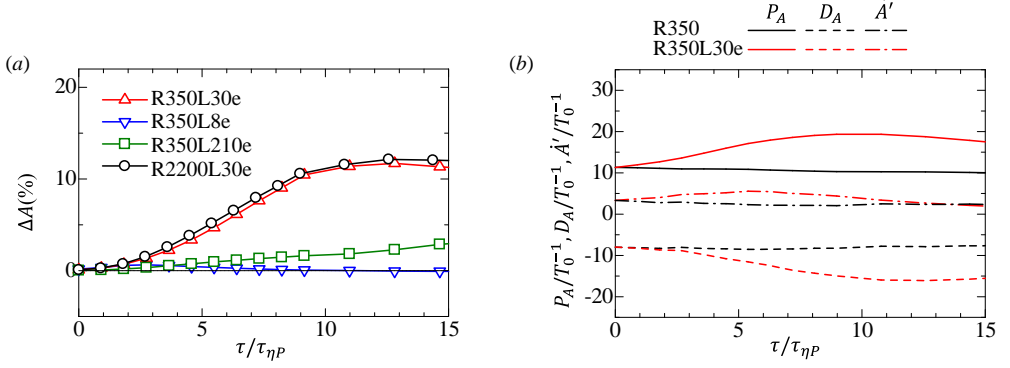


Figure 8: (a) Relative change in the scalar isosurface area  $A$  due to external perturbations, denoted as  $\Delta A$ . (b) Production and destruction terms of the normalised surface area  $A'$  and their balance  $\dot{A}'$ , described by (3.4), in R350 and R350L30e.

30 and  $u_f/u_{\eta P} = 1.4$ . Watanabe & Nagata (2023) investigated the effects of perturbations on decaying isotropic turbulence using the same approach as the present study. Perturbations with  $\lambda_f/\eta_P = 30$  resulted in an increase in the number of vortices generated by the instability of small-scale shear layers. The increase ratio remained consistent across different Reynolds number cases when  $u_f/u_{\eta P}$  was held constant. This behaviour aligns with the comparable increase in  $\dot{V}_S$  and  $A$  observed for R350L30e and R2200L30e.

A similar influence of the promoted instability was reported for turbulent entrainment, whose rate increases when the small-scale shear layers become unstable by internal perturbations (Watanabe 2024a). The entrainment rate is defined as the surface integral of the propagation velocity of the enstrophy isosurface (Holzner & Lüthi 2011). Enhanced entrainment is attributed to an enlarged isosurface area and an increased mean propagation velocity of the enstrophy isosurface, both contributing comparably to the increase in the entrainment rate. In contrast, for the growth rate of the scalar mixing layer, the increase in surface area predominates. Therefore, the enhancements in the entrainment rate and the growth rate of the scalar mixing layer are driven by different mechanisms. The small-scale shear instability promoted by internal perturbations amplifies enstrophy production due to vortex stretching (Watanabe & Nagata 2023), which potentially enhances enstrophy diffusion from turbulent to non-turbulent regions, thereby increasing the mean propagation velocity of the enstrophy isosurface.

The mechanism by which the perturbation increases the surface area can be examined with (3.4). Figure 8(b) presents a comparison between R350 and R350L30e in the temporal variations of the time derivative of the normalised surface area  $\dot{A}' = dA'/dt$  and the two terms  $P_A$  and  $D_A$  in (3.4). The results for R350 indicate that  $P_A > 0$  and  $D_A < 0$  contribute to the production and destruction of surface area, respectively. The roles of  $P_A$  and  $D_A$  align with those observed for the scalar isosurface in a turbulent mixing layer (Blakeley *et al.* 2023). Even without perturbations,  $P_A$  exceeds  $D_A$ , resulting in an increase in surface area over time. The introduction of perturbations that lead to small-scale shear instability affects both terms significantly. Initially,  $P_A$  increases compared to the baseline case, followed by a rise in the magnitude of  $D_A$ . The faster increase in  $P_A$  leads to an increase in the surface area with large  $\dot{A}'$  in R350L30e. It is suggested that the enhanced shear instability excites small-scale turbulent motions (Watanabe & Nagata 2023), which in turn amplify the velocity gradients contributing to  $P_A$ . Consequently, the increase in the surface area is explained by the surface deformation at small scales. This deformation results in a more complex geometry of the

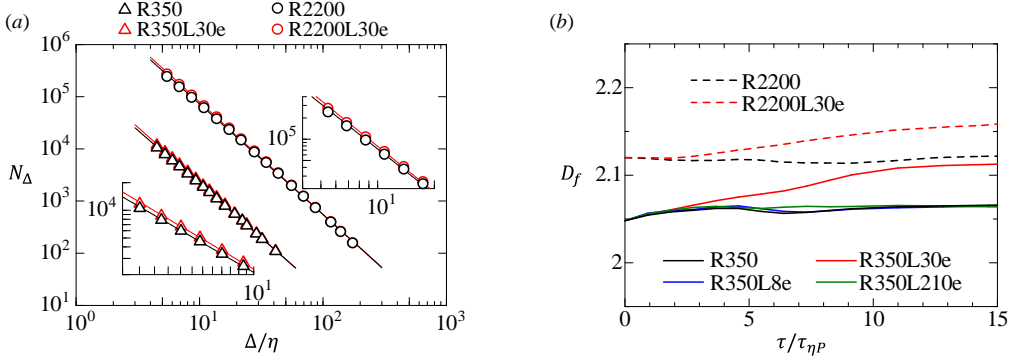


Figure 9: (a) Plots of the number of boxes,  $N_\Delta$ , required to cover the scalar isosurface at  $\tau/\tau_{\eta P} = 13$  for R350, R350L30e, R2200 and R2200L30e, with box size  $\Delta$ . (b) Temporal variations of the fractal dimension  $D_f$ , evaluated by fitting the power law  $N_\Delta \sim \Delta^{-D_f}$ .

surface, affecting the destruction term  $D_A$ , defined with the divergence of the surface normal vector  $\partial n_i / \partial x_i$ , at a later time.

The scalar isosurface in turbulence exhibits fractal properties, crucial for understanding the scaling of its surface area. This study evaluates the fractal dimension  $D_f$  of the scalar isosurface using a three-dimensional box-counting method, which counts the number of cubic boxes,  $N_\Delta$ , required to cover the surface as a function of the box size  $\Delta$ . The calculation of  $N_\Delta$  is performed separately for the scalar isosurfaces on the  $y > 0$  and  $y < 0$  sides. The fractal dimension is determined as the power-law exponent in the plot of  $N_\Delta(\Delta)$ . Figure 9(a) compares  $N_\Delta(\Delta)$  between the baseline cases and the perturbed cases with the unstable wavelength of small-scale shear layers. The lines represent the power law  $N_\Delta \sim \Delta^{-D_f}$ , evaluated using a least squares method. For both Reynolds numbers, deviations in the perturbed cases from the baselines become more prominent as the scale decreases. Specifically,  $N_\Delta$  increases at small scales when the perturbations are introduced, with an increase of about 10% for  $\Delta/\eta < 15$  from the baseline. These results indicate that the promoted small-scale shear instability leads to a more complex geometry of the scalar isosurface at smaller scales. This complexity is consistent with the enhanced effects of surface deformation by velocity gradients observed in figure 8(b).

The fractal dimension  $D_f$  is determined by fitting a power law function to the plot of  $N_\Delta(\Delta)$ . The fractal dimension can slightly vary depending on the fitting range. However, the analysis applies the fitting to all data points shown in figure 9(a). This approach is chosen to focus primarily on examining the perturbation effects on  $D_f$  rather than pinpointing the precise values of  $D_f$ . Figure 9(b) illustrates the temporal variations of  $D_f$ . In the absence of perturbations,  $D_f \approx 2.06$  and  $2.12$  are observed for R350 and R2200, respectively. The introduction of perturbations with the unstable wavelength of small-scale shear layers in R350L30e and R2200L30e results in an increase in  $D_f$ . Such increases are not observed for perturbations with other wavelengths in R350L8e and R350L210e. At  $\tau/\tau_{\eta P} = 15$ ,  $D_f$  reaches approximately 2.11 in R350L30e and 2.16 in R2200L30e, which represent an increase of about 2% over the baseline cases. While this relative increase in  $D_f$  may not seem as substantial as those observed for other quantities, such as  $\Delta \dot{V}_S$ , it is critically important for the surface area  $A$ . This is because  $D_f$  appears as an exponent in the scaling of  $A$ , expressed as  $A \sim \mathcal{L}^{D_f-2}$ , where  $\mathcal{L}$  represents the ratio between the length scale of large-scale motions and the Kolmogorov scale (Meneveau & Sreenivasan 1990). Therefore, even a slight increase

in  $D_f$  can have a significant impact on the surface area, enhancing the scalar transfer and mixing near the boundary.

The scalar isosurfaces in the baseline cases essentially delineate the TNTI layer, a subject of considerable interest in prior studies. It has been established that the enstrophy isosurface near the outer boundary of the TNTI layer closely aligns with the scalar isosurface at  $Sc = 1$ , in terms of both geometry and location, particularly when the scalar threshold is appropriately selected (Gampert *et al.* 2014; Watanabe *et al.* 2018). Therefore, the values of  $D_f$  observed for R350 and R2200 should be comparable to those reported for the TNTI layer. The  $D_f$  value associated with Kolmogorov scaling, 2.33, has been observed in fully developed intermittent turbulent flows (Sreenivasan *et al.* 1989; Mistry *et al.* 2016, 2018; Zhuang *et al.* 2018; Breda & Buxton 2019; Abreu *et al.* 2022; Xu & Long 2023). Other studies have reported smaller  $D_f$  values, around 2.1–2.2 (Zhang *et al.* 2023; Er *et al.* 2023), which have also been observed in the developing regions of jets (Breda & Buxton 2019; Xu & Long 2023). The present DNS results yield  $D_f = 2.05$ –2.12, which is smaller than 2.33. These  $D_f$  values are discussed in relation to the variations noted in previous studies. As shown in figure 9(b),  $D_f$  remains nearly constant over time when no perturbations are introduced, indicating that the transient behaviour associated with turbulence development, observed in the near field of jets, is irrelevant in this context. The TNTI layer comprises two sublayers (da Silva *et al.* 2014; Taveira & da Silva 2014; van Reeuwijk & Holzner 2014). The outer sublayer, known as the viscous superlayer, is characterised by vorticity dynamics dominated by viscous effects. The inner sublayer, referred to as the turbulent sublayer, is where inviscid vortex stretching occurs actively. The location of the enstrophy isosurface within the layer varies depending on the threshold selected. Consequently, the fractal dimension  $D_f$  of the enstrophy isosurface also increases as the threshold becomes larger. In a turbulent jet, for example,  $D_f$  is reported as small as 2.1 when a low enstrophy threshold is used such that the surface marks the irrotational boundary between the TNTI layer and the irrotational fluid (Er *et al.* 2023). This value is consistent with the present values of  $D_f$ . Furthermore, the present study notes that  $D_f$  increases with the Reynolds number, a trend similarly reported for the enstrophy isosurface within the TNTI layer of turbulent boundary layers (Zhang *et al.* 2023). In addition, the scalar isosurface in isotropic turbulence often shows a decreasing trend in fractal dimension as the iso-scalar value deviates from the mean scalar. When the iso-scalar value significantly differs from the mean scalar value, the fractal dimension is approximately 2 (Iyer *et al.* 2020). In the current study, the scalar isosurface chosen to represent the outer boundary of the scalar mixing layer also substantially deviates from the mean scalar value within the layer. The present values of  $D_f$  close to 2 align with these observations of large scalar-fluctuation values in isotropic turbulence.

The increase in surface area and the associated complex geometry resulting from small-scale shear instability align well with experimental findings concerning the scalar interface of jets and wakes in background turbulence (Kohan & Gaskin 2022; Chen & Buxton 2023). The background turbulence in these studies is fully developed and is characterised by a wide range of motion scales, which is different from the current single-scale perturbations. The effects of this background turbulence on the small-scale geometry could potentially be related to the shear instability observed in this study. However, drawing a definitive conclusion at this stage is challenging due to the multi-scale nature of the background turbulence. As discussed in § 2.3, background turbulence in most experiments typically has a characteristic length scale comparable to the integral scale of primary turbulence. Further experimental studies employing small-scale background turbulence are required to observe the effects of promoted small-scale shear instability on the scalar interface. The scalar interface of the boundary layer subjected to freestream turbulence has also been investigated using DNS (Wu *et al.* 2019). The geometry of the interface differs between transitional and fully developed boundary

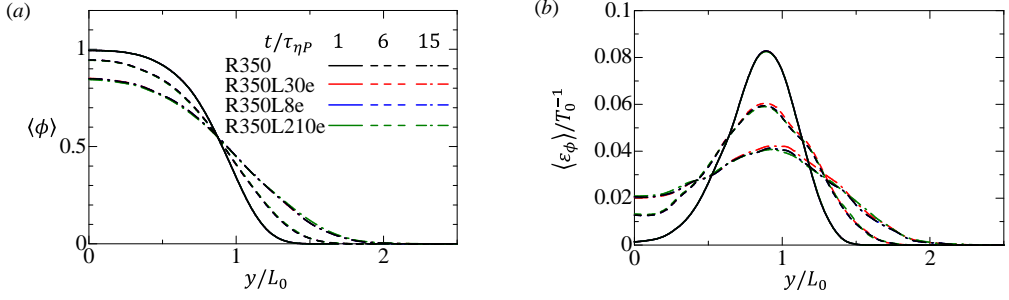


Figure 10: Lateral profiles of scalar statistics in R350, R350L8e, R350L30e and R350L210e: (a) mean scalar  $\langle\phi\rangle$  and (b) mean scalar dissipation rate  $\langle\varepsilon_\phi\rangle$ .

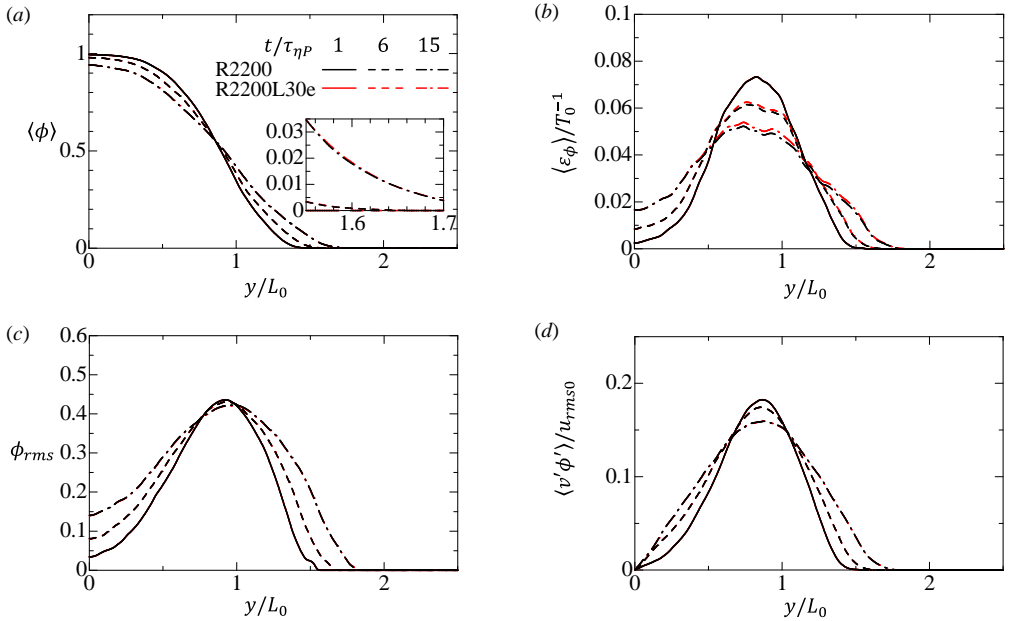


Figure 11: Lateral profiles of scalar statistics in R2200 and R2200L30e: (a) mean scalar  $\langle\phi\rangle$ ; (b) mean scalar dissipation rate  $\langle\varepsilon_\phi\rangle$ ; (c) rms scalar fluctuations  $\phi_{rms}$ ; (d) lateral turbulent scalar flux  $\langle v'\phi'\rangle$ .

707 layers, which exhibit distinct vortical structures near the edge of the boundary layer. The  
 708 influence of freestream turbulence on the interface is expected to depend on the state of the  
 709 primary turbulence.

#### 710 4.3. External perturbation effects on passive scalar statistics

711 Figure 10(a) compares the mean scalar distribution between the perturbed and baseline  
 712 cases. Over time, the scalar mixing layers on both sides develop and eventually reach the  
 713 flow centre, as confirmed by  $\langle\phi\rangle < 1$  at  $y = 0$ . The scalar mixing layer expands in the  $y$   
 714 direction, resulting in an increase in  $\langle\phi\rangle$  over time at larger  $y$  values. Notably, the mean scalar  
 715 distribution remains largely unaffected by perturbations. Figure 10(b) provides a comparison  
 716 for the mean scalar dissipation rate,  $\langle\varepsilon_\phi\rangle = \langle D\nabla\phi \cdot \nabla\phi \rangle$ . In the case of R350L30e, where  
 717 small-scale shear instability is excited, a slight increase in the dissipation peak is observed at  
 718  $\tau/\tau_{\eta P} = 6$  and 15. The development of the mean scalar is dominated by turbulent scalar flux,

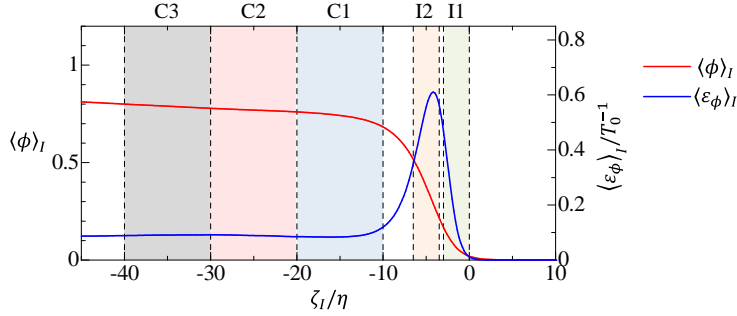


Figure 12: Conditional profiles of mean scalar  $\langle \phi \rangle_I$  and mean scalar dissipation rate  $\langle \varepsilon_\phi \rangle_I$  at  $\tau = 0$  in R2200.

largely contributed by large-scale turbulent motions. The negligible effects of perturbations on  $\langle \phi \rangle$  suggest that the promoted shear instability does not significantly alter large-scale motions. However, the slight increase in  $\langle \varepsilon_\phi \rangle$  suggests that the scalar distribution at small scales is affected by the instability.

Figure 11 presents the results for higher  $Re_{L0}$  cases, R2200 and R2200L30e, including the rms scalar fluctuations,  $\phi_{rms} = \sqrt{\langle \phi'^2 \rangle}$ , and the lateral turbulent scalar flux,  $\langle v' \phi' \rangle$ . The perturbation effects are consistent across both  $Re_{L0}$  cases. The mean scalar profile remains largely unaffected by the perturbations, while a slight increase in the mean scalar dissipation rate is observed in R2200L30e compared to the baseline case of R2200. Additionally, the rms scalar fluctuations and turbulent scalar flux exhibit negligible differences between the perturbed and unperturbed cases, as shown in figures 11(c) and (d). Figure 11(a) includes an enlarged plot of the mean scalar,  $\langle \phi \rangle$ , near the location where  $\langle \phi \rangle \approx 0.02$ . While the scalar isosurface propagation of  $\phi = 0.02$  is enhanced by external perturbations in R350L30e, the mean scalar profile around  $\langle \phi \rangle \approx 0.02$  remains largely unaffected by the perturbations.

External perturbations are expected to have more pronounced influences near the boundary than in the core region of the scalar mixing layer. This behavior near the boundary cannot be captured by the conventional statistics defined by spatial averages, which tend to focus more on the bulk properties of the flow. This issue has been discussed in previous studies of the TNTI layer. Conditional averages of various flow variables, such as velocity and enstrophy, taken relative to the interface location, exhibit a pronounced gradient near the interface (Bisset *et al.* 2002). However, this gradient is not visible in conventional statistics, defined using time averages in statistically steady flows or spatial averages in homogeneous directions. The TNTI layer is thin, with a typical thickness of about 10–20 times the Kolmogorov scale, and occupies only a small fraction of the flow region (da Silva *et al.* 2014). Consequently, the TNTI layer contributes minimally to conventional statistics, which are predominantly influenced by flow regions far away from the TNTI layer. Therefore, the effects of external perturbations on the boundary region of the scalar mixing layer are expected to be more evident in interface-based statistics than in the conventional statistics examined in figures 10 and 11. For this reason, the present exploration is further extended by employing conditional statistics near the outer boundary of the scalar mixing layer. The analysis of perturbation effects using conditional statistics near the outer boundary of the scalar mixing layer focuses primarily on cases R2200 and R2200L30e, with the latter featuring perturbations with the unstable wavelength of small-scale shear layers. The dependence on perturbation wavelength and Reynolds number is later discussed with all cases of R350 and R2200.

Figure 12 displays conditional profiles of the mean scalar,  $\langle \phi \rangle_I$ , and the mean scalar



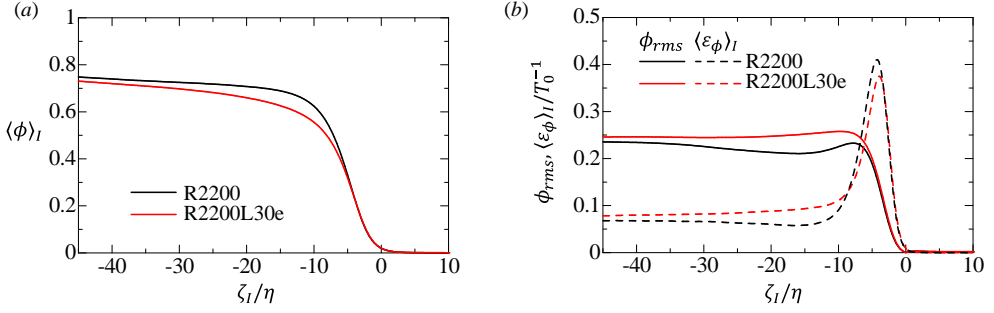


Figure 13: External perturbation effects on conditional statistics at  $\tau/\tau_{\eta P} = 13$  in R2200 and R2200L30e: (a) mean scalar and (b) rms scalar fluctuation and mean scalar dissipation rate.

dissipation rate,  $\langle \varepsilon_\phi \rangle_I$ , in R2200 without perturbations. The profiles exhibit typical behaviors observed in intermittent flows, similar to those studied for understanding mixing near the TNTI layer (Westerweel *et al.* 2009; Gampert *et al.* 2014; Watanabe *et al.* 2015b; Mistry *et al.* 2016; Zhang *et al.* 2019; Kohan & Gaskin 2020). In these profiles,  $\langle \phi \rangle_I$  sharply decreases to zero within a thin interfacial layer about  $10\eta$  thick, while exhibiting a slow increase in the core region of the scalar mixing layer, where  $\zeta_I/\eta \lesssim -10$ . The scalar dissipation rate peaks within this interfacial layer due to the scalar gradient across the layer. To delve deeper into the temporal variations of these conditional statistics, spatial averages are also taken within defined subregions labeled as I1, I2 and C1–C3 in figure 12. The outer part of the interfacial layer,  $-3.0 \leq \zeta_I/\eta \leq 0$ , is designated as I1, while the region containing the peak in the scalar dissipation rate,  $-6.0 \leq \zeta_I/\eta \leq -3.5$ , is defined as I2. These ranges of  $\zeta_I$  are chosen based on the location of the dissipation peak. The core regions of the scalar mixing layer are denoted by C1, C2 and C3, sequentially moving away from the interfacial layer from C1 to C3. The core region is statistically nearly homogeneous, as the shear-free turbulent front originates from HIT. This contrasts with I1 and I2, where the mean scalar rapidly decreases from the inside to the outside of the scalar mixing layer. Due to the small spatial variations of statistics with  $\zeta_I$  in the core region, C1, C2 and C3 are separated by a constant spacing of  $10\eta$ , ranging from  $\zeta_I/\eta = -10$  to  $-40$ . The region between I2 and C1 is excluded from this temporal analysis to ensure a clear separation between the two subregions. Averages within each subregion are denoted by  $\bar{f}$ . The rms scalar fluctuation within each subregion is calculated as  $\phi_{rms} = (\overline{\phi^2} - \bar{\phi}^2)^{1/2}$ . The mean scalar dissipation rate is denoted by  $\bar{\varepsilon}_\phi$ . Together, these two quantities define the mixing time scale  $\tau_\phi = \phi_{rms}^2 / \bar{\varepsilon}_\phi$ , which provides insights into how quickly the scalar is mixed within these regions (Fox 2003). These subregions are used exclusively to examine the temporal variations of perturbation effects, while the  $\zeta_I$  dependence of statistics is also captured in the conditional averages presented as functions of  $\zeta_I$ .

Figure 13(a) compares the conditional mean scalar profiles between R2200 and R2200L30e at  $\tau/\tau_{\eta P} = 13$ , an instance at which the development of the scalar mixing layer has already been influenced by promoted small-scale shear instability in R2200L30e. The perturbation in R2200L30e results in a smaller mean scalar compared to R2200. The faster growth of the scalar mixing layer in R2200L30e is linked to enhanced molecular diffusion, which is more effective in transferring scalar outward due to the increased surface area. Additionally, promoting small-scale instability also accelerates the growth of the turbulent front through entrainment (Watanabe 2024a), which draws the outer fluid with smaller  $\phi$  values into the turbulent front. These changes due to the perturbations explain the reduced



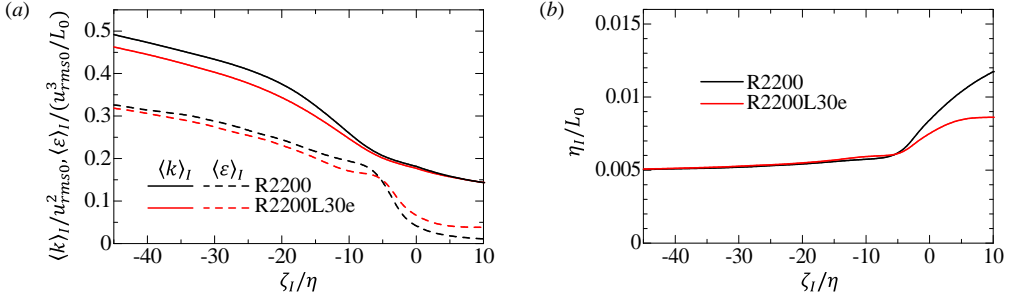


Figure 14: (a) Conditional averages of kinetic energy  $\langle k \rangle_I$  and its dissipation rate  $\langle \varepsilon \rangle_I$  and (b) Kolmogorov scale defined with the conditional statistics,  $\eta_I$ , at  $\tau/\tau_{\eta P} = 13$  in R2200 and R2200L30e.

conditional mean scalar observed in R2200L30e. This reduction in the conditional mean scalar is consistent with findings from studies of TTI layers in a turbulent wake developing in freestream turbulence. The increasing effects of freestream turbulence tend to decrease the conditional mean scalar near the interface (Kankanwadi & Buxton 2020).

Figure 13(b) examines the rms scalar fluctuations  $\phi_{rms} = (\langle \phi^2 \rangle_I - \langle \phi \rangle_I^2)^{1/2}$  and the mean scalar dissipation rate  $\langle \varepsilon_\phi \rangle_I$  at the same time instance as figure 13(a). The perturbations lead to an increase in  $\phi_{rms}$ , explained by a greater amount of entrained fluid with scalar values  $\phi \approx 0$  that differ from those within the scalar mixing layer. Interestingly, the peak in the mean scalar dissipation rate decreases with the perturbations. The scalar gradient within the interfacial layer, dominated by the normal component at the scalar isosurface, is well captured by the mean scalar profile along  $\zeta_I$ , taken in the surface-normal direction. Consequently, the lower mean scalar in the scalar mixing layer in the perturbed case correlates with a smaller dissipation peak within the interfacial layer. Conversely, the scalar dissipation in the core region, where  $\zeta_I/\eta \lesssim -10$ , is increased by the perturbations, as expected from the increase in the rms scalar fluctuations. These conditional statistics reveal more significant perturbation effects on both the mean scalar and mean scalar dissipation rate than conventional statistics in figure 11. The external perturbations predominantly influence the scalar and flow fields near the boundary of the scalar mixing layer. Conventional statistics fail to capture these perturbation effects near the boundary, as they are obscured by contributions from flow regions irrelevant to the boundary region.

The impact of perturbations on the flow field is analysed through conditional averages of kinetic energy and its dissipation rate, defined as  $\langle k \rangle_I = \langle (u^2 + v^2 + w^2)/2 \rangle_I$  and  $\langle \varepsilon \rangle_I = \langle 2\nu S_{ij}S_{ij} \rangle_I$ , respectively. Figure 14(a) presents a comparison of these quantities between R2200 and R2200L30e at  $\tau/\tau_{\eta P} = 13$ . In the core region of the scalar mixing layer ( $\zeta_I/\eta < -10$ ), both kinetic energy and its dissipation rate are reduced due to the perturbations. This reduction is consistent with the enhanced entrainment of outer fluids, which typically possess lower kinetic energy compared to the turbulent front (Taveira & da Silva 2013). The perturbations also appear to have a minimal effect on  $\langle k \rangle_I$  outside the scalar mixing layer, where large-scale motions induced by the turbulent front dominate (da Silva & Pereira 2008). This observation aligns with the nature of the perturbations, which have a small amplitude and decay over time, limiting their ability to significantly alter the large-scale flow. Even without perturbations, the region outside the scalar mixing layer retains non-negligible kinetic energy and dissipation. In R2200, the boundary of the scalar mixing layer approximates the interface separating turbulent and non-turbulent regions (Gampert *et al.* 2014; Watanabe *et al.* 2018). The kinetic energy of this irrotational motion induced by

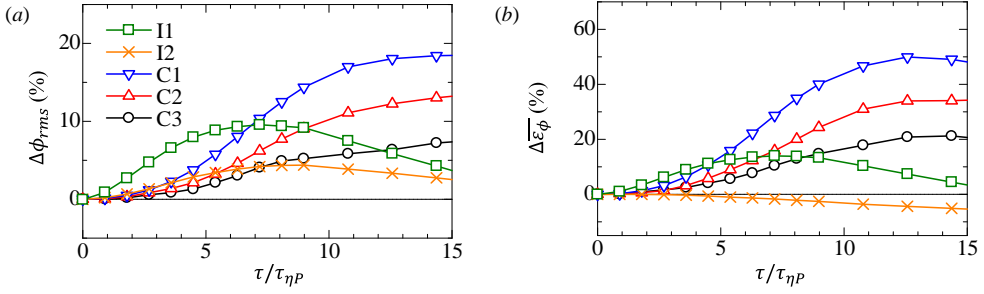


Figure 15: Temporal variations of relative changes at different positions along the  $\zeta_I$  coordinate in R2200L30e: (a) rms scalar fluctuation, denoted as  $\Delta\phi_{rms}$ , and (b) mean scalar dissipation rate, denoted as  $\Delta\bar{\varepsilon}_\phi$ .

turbulence decays with distance from the interface, as theoretically predicted (Phillips 1955; Teixeira & da Silva 2012; Zecchetto *et al.* 2024). This decay is reflected in the decreases of  $\langle k \rangle_I$  and  $\langle \varepsilon \rangle_I$  with increasing  $\zeta_I$ , consistent with observations in other intermittent turbulent flows (Taveira *et al.* 2013; Watanabe *et al.* 2016b; Buxton *et al.* 2019).

Figure 14(b) presents the Kolmogorov scale  $\eta_I = (\nu^3/\langle \varepsilon \rangle_I)^{1/4}$  calculated as a function of  $\zeta_I$ . In the core region, where  $\zeta_I/\eta < -10$ ,  $\eta_I$  is hardly influenced by the perturbations. The changes in  $\langle \varepsilon \rangle_I$  are not significant enough to substantially affect the local Kolmogorov scale within the scalar mixing layer. The Kolmogorov scale increases for  $\zeta_I > 0$ , corresponding to the region outside the scalar mixing layer. This increase is directly associated with the decay in the kinetic energy dissipation rate discussed above. In studies of the TNTI layer in turbulent boundary layers, it has been shown that the area of the surface delineating the outer boundary of the TNTI layer scales as  $\delta_{BL}^2 (\delta_{BL}/\eta_I)^{D_f-2}$ , where  $\delta_{BL}$  is the boundary layer thickness and  $\eta_I$  is taken from the turbulent core region near the TNTI layer (Zhang *et al.* 2023). Perturbations have minimal impact on  $\eta_I$  in the core region of the scalar mixing layer. Additionally, the lateral profile of mean scalar remains largely unaffected by the perturbations, indicating that the length scale of large-scale motions is also not influenced by perturbations. Thus, the changes in characteristic length scales due to perturbations contribute minimally to the observed increase in the scalar isosurface area. This increase is instead dominated by the rise in the fractal dimension, highlighting how geometric complexity, rather than changes in turbulent scales, primarily drives the expansion of the surface area in this case.

Figure 15(a) illustrates the relative changes in rms scalar fluctuation, denoted as  $\Delta\phi_{rms}$ , caused by perturbations in R2200L30e. The results, evaluated across five subregions depicted in figure 12, are plotted over time. Notably, the perturbations result in an increase in  $\phi_{rms}$  across all positions near the outer boundary. The increase in  $\Delta\phi_{rms}$  initially begins within the interfacial layer, specifically in I1, which represents the outer part of this layer. It is important to note that I1 has very small  $\phi_{rms}$ , and therefore its increase, indicated by a large  $\Delta\phi_{rms}$ , is not distinctly visible in figure 13(b). Within the core region of the scalar mixing layer, the increase in  $\phi_{rms}$  is most pronounced in C1 and diminishes towards C3.

Figure 15(b) shows the relative changes in the mean scalar dissipation rate,  $\Delta\bar{\varepsilon}_\phi$ , for each subregion. The temporal variations of  $\Delta\bar{\varepsilon}_\phi$  align with those of  $\Delta\phi_{rms}$ . The increase in  $\bar{\varepsilon}_\phi$  also starts from I1, near the boundary of the scalar mixing layer. The mean scalar dissipation rate does not increase within I2, which is the peak location of the conditional mean scalar dissipation rate. Here,  $\bar{\varepsilon}_\phi$  slightly decreases over time, as indicated by a negative  $\Delta\bar{\varepsilon}_\phi$ . However, near the interfacial layer in C1, there is a significant increase in  $\bar{\varepsilon}_\phi$ , with a relative increase of about 50%. This effect progressively diminishes moving away from the boundary, from C1 to C3. These observations from figure 15 underscore that while perturbations

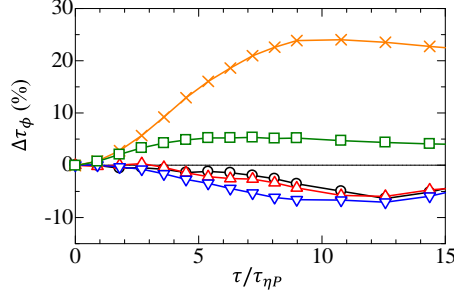


Figure 16: Temporal variations of relative changes in the mixing time scale at different positions along the  $\zeta_I$  coordinate in R2200L30e. The symbols are the same as in figure 15.

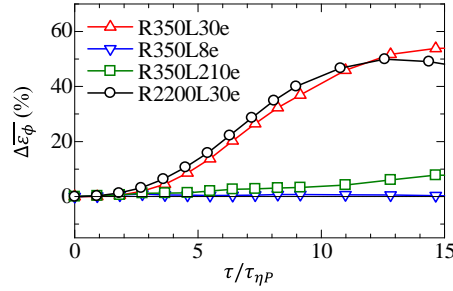


Figure 17: Temporal variations of relative changes in the mean scalar dissipation rate  $\Delta\overline{\varepsilon}_\phi$  in C1, across different perturbation wavelengths and Reynolds numbers.

enhance scalar fluctuations and dissipation rates near the boundary, their influence is not uniform across the scalar mixing layer. The scalar mixing processes near the outer boundary are particularly sensitive to these external perturbations.

Figure 16 presents the relative changes in the mixing time scale, denoted as  $\Delta\tau_\phi$ . In the subregions I1 and I2, which are within the interfacial layer,  $\tau_\phi$  increases under the influence of the perturbations, indicating a slower mixing process due to the diffusive effects. Here,  $\tau_\phi$  defines a local time scale, which does not take into account the spatial distribution of the scalar. Despite the locally slower mixing, the overall efficacy of outward scalar diffusion in the interfacial layer is enhanced due to the enlarged surface area, as evidenced by the increased growth rate of the scalar mixing layer. Conversely, in the core region of the scalar mixing layer, a locally faster mixing is observed, characterised by smaller  $\tau_\phi$  or negative  $\Delta\tau_\phi$ .

Figure 17 compares the relative changes in the mean scalar dissipation rate within subregion C1 among 4 cases. Regardless of the Reynolds numbers, perturbations with the unstable wavelength of small-scale shear layers result in a significant increase in the scalar dissipation rate. In both R350L30e and R2200L30e,  $\Delta\overline{\varepsilon}_\phi$  reaches 50%, showing substantial enhancement even with a smaller perturbation energy in R2200L30e. The rate of increase in  $\Delta\overline{\varepsilon}_\phi$  is similar for both cases when time is normalised by the Kolmogorov time scale, suggesting that a similar enhancement of the scalar dissipation rate is achievable at different Reynolds numbers. In contrast, perturbations at other wavelengths are less effective, as shown by the small variations in  $\Delta\overline{\varepsilon}_\phi$ .

The above results confirm that the growth rate of the scalar mixing layer and small-scale scalar mixing near the boundary are enhanced by perturbations with a wavelength of approximately  $30\eta_P$ . The wavelength dependence of these effects is thoroughly investigated by examining the series of R350 with external perturbations with varying wavelength

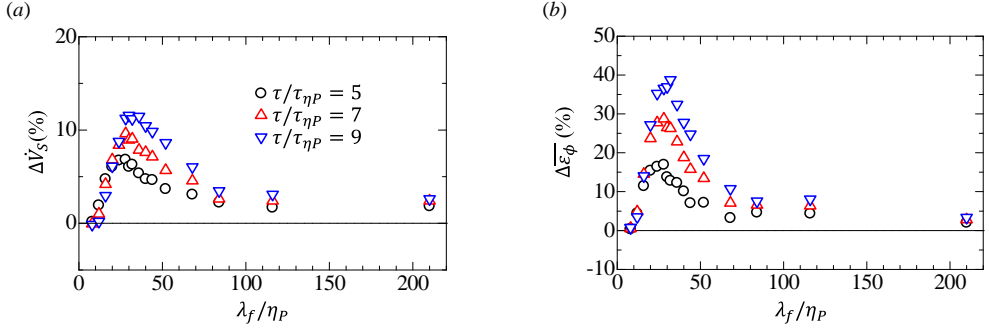


Figure 18: The wavelength dependence of perturbation effects on (a) the growth rate of the scalar mixing layer,  $\Delta \dot{V}_S$ , and (b) the mean scalar dissipation rate near the interface in C1,  $\Delta \overline{\varepsilon}_\phi$ . Results are compared across the series of R350 with external perturbations for all tested wavelength values.

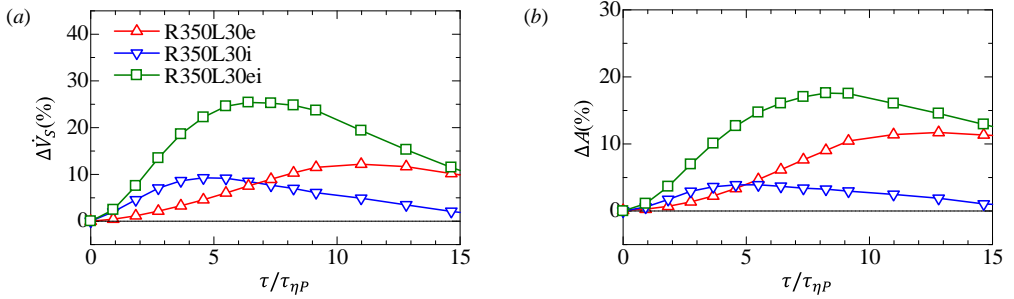


Figure 19: Relative changes due to perturbations introduced in different flow regions in R350L30e, R350L30i and R350L30ei: (a) the growth rate of the scalar mixing layer,  $\dot{V}_S$  and (b) the area  $A$  of the scalar isosurface.

parameters. Figure 18(a) plots the relative change in the growth rate,  $\Delta \dot{V}_S$ , as a function of wavelength  $\lambda_f$ , at three time instances, while figure 18(b) presents the corresponding results for the mean scalar dissipation rate near the boundary,  $\Delta \overline{\varepsilon}_\phi$ , calculated in C1. Temporal variations for selected  $\lambda_f$  cases have been shown in figures 7(b) and 17. The results indicate peaks in  $\Delta \dot{V}_S$  and  $\Delta \overline{\varepsilon}_\phi$  for  $28 \lesssim \lambda_f/\eta_P \lesssim 35$ . This range aligns with the most unstable wavelength predicted by the shear layer model and the statistics of shear layers in isotropic turbulence (Watanabe & Nagata 2023). The peak wavelength slightly increases over time, likely due to the increase in the Kolmogorov scale, which rises by 30% from the perturbation introduction to the end of the simulation. The effects of perturbations diminish as  $\lambda_f$  deviates from the peak wavelength, with smaller  $\lambda_f$  resulting in a more rapid decline compared to larger  $\lambda_f$ . This behaviour is consistent with the faster decay of small-scale perturbations in figure 5. Perturbations with wavelengths slightly different from the peak wavelength still enhance the growth rate and scalar dissipation rate. For individual shear layers, the most unstable wavelength depends on the thickness. While the probability density function of shear layer thickness peaks at  $4\eta$  in isotropic turbulence, the full width at half maximum is also about  $4\eta$  (Watanabe & Nagata 2023), leading to variations in the most unstable wavelength. Consequently, perturbations remain effective in influencing the shear layers even when the wavelength slightly deviates from  $\lambda_f = 30\eta_P$ .

#### 4.4. Dependence on perturbation locations

The effects of perturbations on passive scalar statistics are compared across different perturbation locations in the R350L30e, R350L30i and R350L30ei cases, where perturbations with the unstable wavelength of small-scale shear layers are applied. For internal perturbations, changes in the flow field due to perturbation-induced shear instability, such as the number of vortices and other turbulent statistics, have been detailed for decaying HIT in our previous study (Watanabe & Nagata 2023).

Figure 19(a) compares the relative changes in the growth rate of the scalar mixing layer,  $\Delta\dot{V}_S$ , among R350L30e, R350L30i and R350L30ei. All cases exhibit an enhanced growth rate, with the perturbation effects appearing more rapidly when introduced inside the turbulent region, as seen in R350L30i and R350L30ei. The promoted shear instability, observed in figure 6, occurs within the turbulent front. In R350L30i and R350L30ei, the perturbations are introduced within the turbulent region, where the shear layers are present, and are expected to immediately influence the evolution of the shear layers. External perturbations do not alter the shear layers early on because they are introduced outside where no shear layers exist. Perturbations in R350L30e and R350L30i are bounded by the scalar isosurface used to evaluate  $\dot{V}_S$ . The differing timescales in the increase in  $\dot{V}_S$  between these cases confirm that the perturbations themselves do not directly cause the increase in growth rate. Instead, it occurs through the excitement of small-scale shear instability, as visualised in figure 6(b). All cases also show a decrease in  $\Delta\dot{V}_S$  after the peak, but the initial increase lasts longer for external perturbations in R350L30e. Internal perturbations evolve within the turbulent flow. Though internal perturbations introduce a peak in the kinetic energy spectrum at the perturbation wavelength, this peak decays rapidly in turbulence due to energy transfer toward smaller scales and energy dissipation (Watanabe & Nagata 2023). Conversely, external perturbations introduced outside the turbulence can maintain their length scale, leading to more pronounced effects even later. This difference may lead to a larger peak value of  $\Delta\dot{V}_S$  for external perturbations in R350L30e compared to internal perturbations in R350L30i. Furthermore, the most significant increase in the growth rate is observed in R350L30ei, where perturbations are introduced across the entire flow region. The timing of the peak in  $\Delta\dot{V}_S$  lies between those of R350L30i and R350L30e, as both internal and external perturbations influence the growth rate in R350L30ei.

Figure 19(b) shows the relative change in the area,  $\Delta A$ , of the scalar isosurface. Unlike the external perturbations used in R350L30e, the peak values of  $\Delta A$  and  $\Delta\dot{V}_S$  differ when perturbations are introduced inside the turbulent region (R350L30i and R350L30ei). In these cases, the peaks of  $\Delta\dot{V}_S$  are larger than those of  $\Delta A$ , indicating that internal perturbations also enhance the local propagation velocity of the outer boundary of the scalar mixing layer.

Figure 20 presents the fractal dimension  $D_f$  for R350, R350L30e, R350L30i and R350L30ei. Regardless of the perturbation location, the perturbations result in an increase in  $D_f$ , indicating a more complex surface geometry. Similar to the observations for  $\Delta\dot{V}_S$  and  $\Delta A$ , the effects of internal perturbations in R350L30i diminish more rapidly compared to external ones. Initially, internal perturbations cause a greater increase in  $D_f$ , which correlates with a larger initial increase in the growth rate of the scalar mixing layer. Perturbations introduced across the entire flow region have the most significant impact on the fractal dimension of the scalar isosurface. The correlation between the increases in  $D_f$  and  $\Delta\dot{V}_S$  further underscores that the enhanced surface complexity, driven by shear instability, plays a significant role in the increased growth rate of the scalar mixing layer.

Figure 21(a) illustrates the temporal variations of the production ( $P_A$ ) and destruction ( $D_A$ ) terms in the isosurface-area equation (3.4). When perturbations are introduced,  $P_A$  increases rapidly. Then, the increase in  $D_A$  follows with a delay relative to the increase in  $P_A$ .

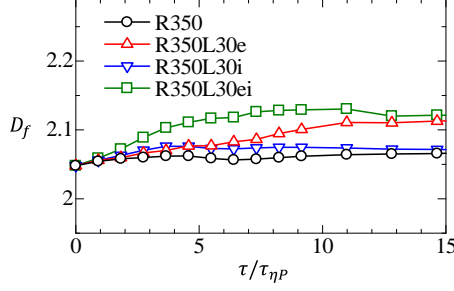


Figure 20: Temporal variations in the fractal dimension  $D_f$  of the scalar isosurface defining the outer boundary of the scalar mixing layer in R350, R350L30e, R350L30i and R350L30ei.

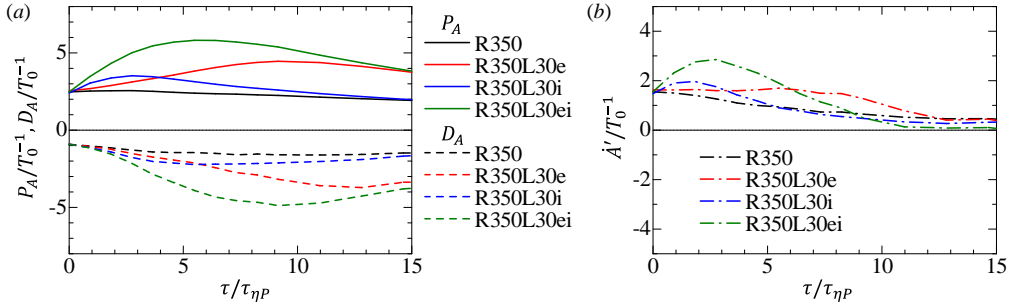


Figure 21: Production and destruction terms of the normalised surface area  $A'$ , as described by (3.4), in R350, R350L30e, R350L30i and R350L30ei: (a) production ( $P_A$ ) and destruction ( $D_A$ ) terms of the isosurface area; and (b) their balance ( $\dot{A}'$ ).

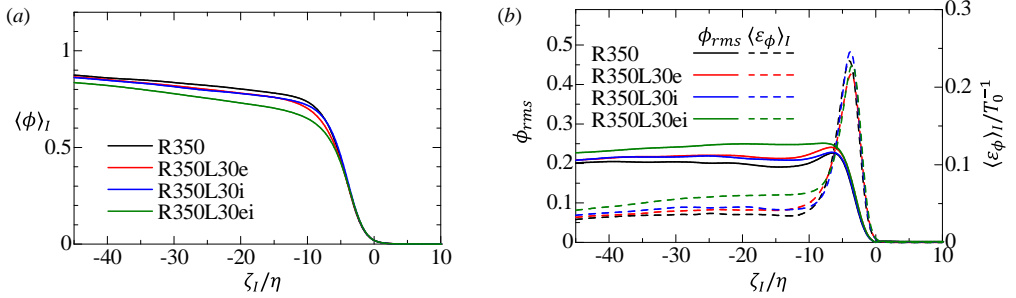


Figure 22: Conditional profiles of (a) mean scalar  $\langle \phi \rangle_I$  and (b) rms scalar fluctuation  $\phi_{rms}$  and mean scalar dissipation rate  $\langle \epsilon_\phi \rangle_I$  at  $\tau/\tau_{\eta P} = 7.5$  in R350, R350L30e, R350L30i and R350L30ei.

Consequently, the isosurface area increases when perturbations are introduced. This is further confirmed in figure 21(b), which compares  $\dot{A}' = P_A + D_A$  across the four simulation cases. In R350L30i and R350L30ei, where perturbations are introduced within the turbulent region,  $\dot{A}'$  shows a rapid increase compared to R350L30e with external perturbations, resulting in a faster initial growth rate of the scalar mixing layer.

Figure 22(a) compares the conditional mean scalar at  $\tau/\tau_{\eta P} = 7.5$ . At this time, the growth rate of the scalar mixing layer has increased by approximately 7% in R350L30e and R350L30i, and by about 25% in R350L30ei, due to the perturbations. Perturbations lead to a

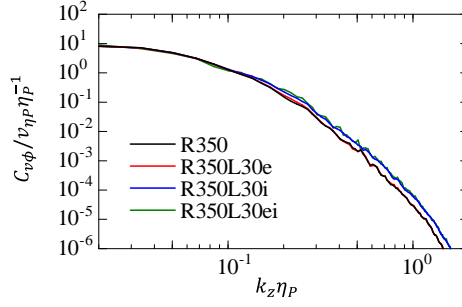


Figure 23: Cospectrum of lateral velocity and passive scalar,  $C_{v\phi}$ , at  $y/L_0 = 0.9$  in the scalar mixing layer at  $\tau/\tau_{\eta P} = 7.5$  for R350, R350L30i, R350L30e and R350L30ei. The cospectrum and wavenumber in the  $z$  direction,  $k_z$ , are normalised by the Kolmogorov length and velocity scale at the flow centre at the time of perturbation introduction.

decrease in the mean scalar, aligning with expectations from the enhanced growth rate of the scalar mixing layer. However, internal perturbations in R350L30i sustain a sharp mean scalar gradient within the interfacial layer. This region experiences molecular diffusion transferring scalar from inside to outside the scalar mixing layer, typically smearing the distinct scalar distribution jump. Previous studies have shown that small-scale turbulent scalar transport to the interfacial layer helps sustain this scalar jump (Watanabe *et al.* 2015*b,a*). The mean scalar gradient similar to the baseline case could be maintained by small-scale turbulent motion in the turbulent core region, which is amplified by the shear instability induced by internal perturbations. This is confirmed below with a velocity and scalar cospectrum. In the R350L30ei case, where perturbations are introduced throughout the entire flow region, a significant increase in the growth rate of the scalar mixing layer is observed. This leads to a notable decrease in the mean scalar within the mixing layer, resulting in a less steep mean scalar gradient within the interfacial layer compared to R350L30i.

Figure 22(*b*) displays the rms scalar fluctuation ( $\phi_{rms}$ ) and mean scalar dissipation rate ( $\langle \varepsilon_\phi \rangle_I$ ) near the outer boundary. The effects of both internal and external perturbations manifest similarly in the core region of the scalar mixing layer, with increases in both  $\phi_{rms}$  and  $\langle \varepsilon_\phi \rangle_I$ . However, the reduction in the dissipation peak observed with external perturbations (R350L30e) does not occur with internal perturbations (R350L30i). This distinction is due to the internal perturbations maintaining a sharp scalar gradient within the interfacial layer in figure 22(*a*). Further detailed comparisons for these perturbations are provided below with the analysis within each subregion on  $\zeta_I$ . R350L30ei with perturbations in the entire flow region exhibits the most significant increase in the rms scalar fluctuation ( $\phi_{rms}$ ) and mean scalar dissipation rate in the core region, corresponding to the most substantial rise in the growth rate of the scalar mixing layer.

Figure 23 examines the cospectrum of lateral velocity and passive scalar,  $C_{v\phi}$ , calculated with Fourier transform in the  $z$  direction. This cospectrum, when integrated over the wavenumber  $k_z$ , represents the turbulent scalar flux and is assessed for potential enhancements of the turbulent scalar transport due to internal perturbations. Here,  $C_{v\phi}$  is taken at  $y/L_0 = 0.9$  and  $\tau/\tau_{\eta P} = 7.5$ . The observed increase in  $C_{v\phi}$  at small scales in R350L30i and R350L30ei indicates enhanced scalar transport due to small-scale shear instabilities. However, the total turbulent flux, represented by  $\langle v'\phi' \rangle$ , is primarily influenced by larger scales, where  $C_{v\phi}$  remains largely unaffected by perturbations. This finding implies that the observed changes in  $C_{v\phi}$  at smaller scales are not sufficient to alter the mean scalar profile across the scalar mixing layer significantly. However, the turbulent scalar transport near the outer boundary of the scalar mixing layer is predominantly driven by small-scale



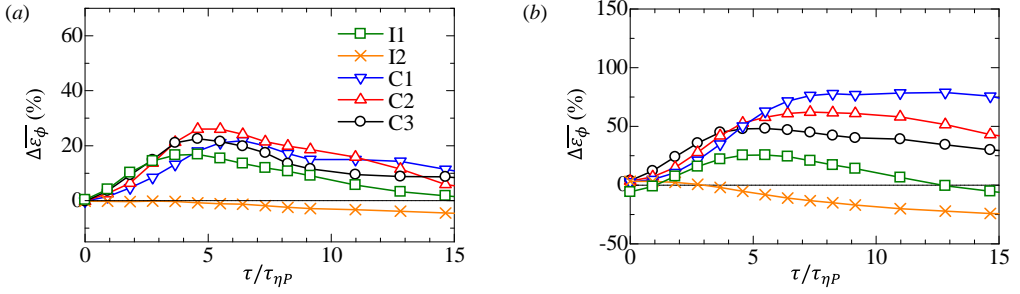


Figure 24: Relative changes in the mean scalar dissipation rate,  $\Delta\overline{\varepsilon}_\phi$ , across various subregions near the outer boundary of the scalar mixing layer in (a) R350L30i and (b) R350L30ei.

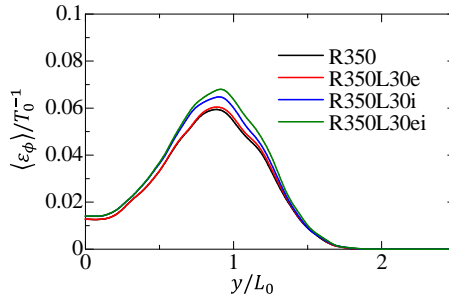


Figure 25: Lateral profiles of mean scalar dissipation rate,  $\langle\varepsilon_\phi\rangle$ , at  $\tau/\tau_{\eta P} = 7.5$  in R350, R350L30e, R350L30i and R350L30ei.

velocity fluctuations, which are represented as a velocity difference between two points with a small separation in the local scalar transport equation (Watanabe *et al.* 2014a, 2015b). Consequently, the enhanced  $C_{v\phi}$  at small scales can still influence the mean scalar profile near the boundary where internal perturbations maintain a sharp mean scalar gradient in R350L30i. In contrast, external perturbations do not affect  $C_{v\phi}$  because their influence is confined to the vicinity of the boundary. This aligns with the observation of a smaller mean scalar gradient near the boundary in R350L30e as shown in figure 22(a).

Figure 24(a) displays the relative changes in the mean scalar dissipation rate due to internal perturbations (R350L30i) in each subregion on the  $\zeta_I$  coordinate. The results demonstrate an almost uniform increase in scalar dissipation rate of 20–30% across C1–C3 compared to the baseline case (R350). This uniform effect contrasts with external perturbations, whose impact on the scalar dissipation rate drastically decreases from C1 to C3, as shown in figure 15(b). However, external perturbations typically lead to a more significant increase in the mean scalar dissipation rate, as also discussed above for the growth rate of the scalar mixing layer. Figure 24(b) shows the results for perturbations introduced throughout the entire flow region in R350L30ei. Inside the scalar mixing layer near the interface, the mean scalar dissipation rate increases significantly, with the increase ratio ranging from 50% to 75% across subregions C1 to C3. The perturbation effects diminish progressively from C1 to C3 with increasing distance from the boundary. This behaviour is consistent with the influence of external perturbations in R350L30e, shown in figure 15(b).

Figure 25 compares the lateral profiles of the mean scalar dissipation rate,  $\langle\varepsilon\rangle$ , at  $\tau/\tau_{\eta P} = 7.5$ . The profiles indicate that internal perturbations in R350L30i and R350L30ei influence small-scale mixing in the entire region, resulting in a significant increase in the mean scalar

dissipation rate. In contrast, the effects of external perturbations in R350L30e are largely restricted to the vicinity of the outer boundary of the scalar mixing layer. As a result, the mean scalar dissipation rate, which is predominantly influenced by the internal region of the scalar mixing layer, is only minimally affected by external perturbations in figure 25. This distinction underscores how internal and external perturbations differentially influence turbulence. Exciting small-scale shear instability internally leads to widespread enhancements in small-scale mixing throughout the turbulent region, while external perturbations enhance mixing near the boundary. The enhanced scalar dissipation rate resulting from the perturbations has significant implications for the turbulent mixing mechanism. This type of instability can occur even without perturbations, while the introduction of perturbations accelerates the process, intensifying the effects. The observed perturbation effects imply the important role of small-scale shear instability in the rapid small-scale mixing facilitated by turbulent motions.

## 5. Conclusions

The DNS of a turbulent front with passive scalar transfer has revealed significant impacts of perturbations with the unstable wavelength of small-scale shear layers, about 30 times the Kolmogorov scale, on scalar mixing in turbulence. The present study has tested perturbations, which are introduced locally, either inside or outside the turbulent front, or globally throughout the entire flow field. Here, velocity perturbations are superimposed on the flow at a given instance, and the subsequent flow evolutions are compared between the perturbed and unperturbed cases. The perturbations are introduced to the turbulent front, with the turbulent Reynolds numbers based on the Taylor microscale of 72 or 202. The scalar mixing layer in the turbulent front develops in space by the outward diffusion, which takes place at the outer boundary of the scalar mixing layer. Such perturbations enhance shear layer instability even near the boundary. Perturbations of other wavelengths, however, do not excite this instability, and the associated changes summarised below are less noticeable.

One key effect of the promoted instability is the complex small-scale geometry it induces at the outer boundary, delineated by a scalar isosurface, leading to an increase in the fractal dimension of the surface. This geometric alteration expands the surface area, enhancing scalar diffusion from inside to outside the scalar mixing layer. Consequently, the mean scalar near the boundary is reduced due to efficient diffusion. Moreover, the perturbations contribute to increased scalar fluctuations and higher scalar dissipation rates within the turbulent region. A comparative analysis of external and internal perturbations highlights that the effects of small-scale shear instability are localised to where they occur. External perturbations alter scalar mixing near the boundary, whereas internal perturbations impact the entire turbulent region. In both scenarios, the scalar dissipation rate increases, especially in the core region of the scalar mixing layer. The rise in the scalar dissipation rate reduces the mixing time scale, indicating faster molecular diffusion spurred by the shear instability. The peak of the mean scalar dissipation rate within the interfacial layer decreases with external perturbations due to enhanced outward diffusion that tends to smooth out the scalar gradient. In contrast, this peak remains largely unchanged with internal perturbations, likely because the small-scale turbulent transport is enhanced within the scalar mixing layer. The relative increase in the mean scalar dissipation rate due to perturbations, compared to the baseline simulation, ranges from approximately 20% to 75%, depending on the perturbation locations. Similarly, perturbations lead to increases of 5% to 18% in the scalar isosurface area and 10% to 25% in the growth rate of the scalar mixing layer. Perturbations introduced across the entire flow region result in the most substantial increases in these quantities than those introduced solely within or outside the turbulent region. The effects of perturbations

are qualitatively consistent across different Reynolds numbers, provided the perturbation amplitude  $u_f$  normalised by the Kolmogorov velocity scale  $u_\eta$  remains constant. This study examines turbulence with initial turbulent Reynolds numbers,  $Re_\lambda$ , of 72 and 202. Previous research on perturbation effects in turbulent entrainment has observed similar Reynolds number independence for perturbations with fixed normalised amplitudes,  $u_f/u_\eta$ , in the range of  $40 \lesssim Re_\lambda \lesssim 300$ . These findings suggest that weaker perturbations can effectively enhance mixing at higher Reynolds numbers. However, further studies are necessary to fully confirm this Reynolds number independence at higher  $Re_\lambda$ . The influences of small-scale shear instability underscore its role in turbulent mixing, as this instability occurs even in the absence of perturbations. The instability of small-scale shear layers is crucial in creating the complex geometry of scalar isosurfaces and facilitating rapid turbulent transport and molecular mixing at small scales.

The implications of the current study extend to various relevant flow phenomena, particularly demonstrating the potential of this mixing enhancement methodology in turbulent reacting flows. Under non-premixed conditions, chemical reactions often actively occur within thin zones that align with an isosurface of mixture fraction (Zhdanov & Chorny 2011; Watanabe *et al.* 2013, 2014b). These reaction zones exhibit similarities with the interfacial layer with a large scalar gradient observed in this study. The increase in the scalar isosurface area is expected to similarly influence these reaction zones. Additionally, the rate of fast reaction is proportional to the scalar dissipation rate, as discussed by Bilger (2004). The observed increase in dissipation inside the scalar mixing layer could thus promote faster reactions. When implementing mixing enhancement via small-scale shear instability in practical applications, it is essential to consider that the Kolmogorov scales characterise the velocity and length scales of shear layers, both of which decrease as the Reynolds number increases. As demonstrated in cases R350L30e and R2200L30e and in Watanabe (2024a), weaker perturbations can excite this instability at higher Reynolds numbers, provided that the perturbation wavelength corresponds to the instability wavelength, which also decreases with the Reynolds number. This feature is crucial in applications to large-scale flows, observed in engineering and environmental flows, such as hot air mixing from heat exchangers in an ambient cross flow (Liu *et al.* 2009), where Kolmogorov-scale perturbations can be more feasible to generate than large-scale perturbations.

**Acknowledgements.** The numerical simulations were performed using the high-performance computing systems at the Japan Agency for Marine-Earth Science and Technology and Nagoya University. This work was also supported by a Collaborative Research Project on Computer Science with High-Performance Computing in Nagoya University.

**Funding.** This work was supported by JSPS KAKENHI Grant Number JP22K03903.

**Declaration of interests.** The authors report no conflicts of interest.

**Data availability statement.** The data supporting the findings of this study are available from the corresponding author upon reasonable request.

## Appendix A. The thresholds applied to detect the turbulent front and scalar mixing layer

In most DNS cases conducted in this study, perturbations are introduced either within or outside the turbulent region. A vorticity magnitude threshold is employed to detect the turbulent region, defined as  $\omega/\langle\omega\rangle \geq \omega_{th}$ , where  $\langle\omega\rangle$  represents the mean vorticity magnitude at  $y = 0$ . The threshold  $\omega_{th}$  is determined using a method based on the  $\omega_{th}$ -dependence of the detected turbulent volume, as proposed by Taveira *et al.* (2013) and successfully applied to various turbulent flows (Jahanbakhshi *et al.* 2015; Watanabe *et al.* 2018; Nagata *et al.*

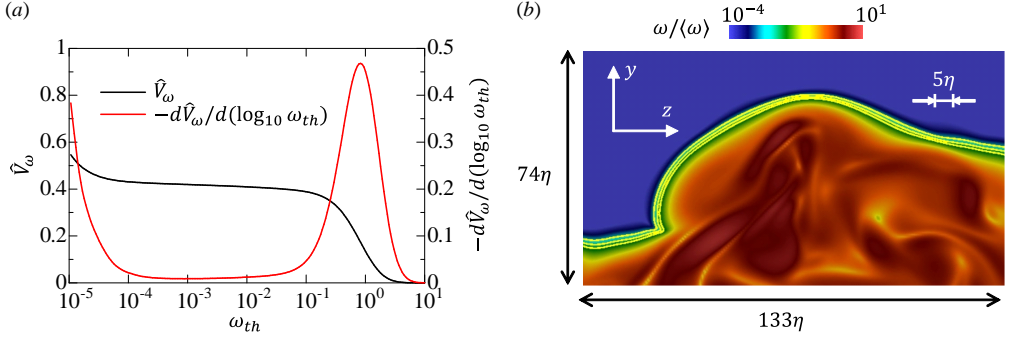


Figure 26: (a) The threshold dependence of the turbulent volume detected as  $\omega/\langle\omega\rangle > \omega_{th}$ , where  $\langle\omega\rangle$  represents the mean vorticity magnitude at  $y = 0$ . The turbulent volume  $V_\omega$  is normalised by the size of the computational domain as  $\hat{V}_\omega = V_\omega/L_x L_y L_z$ . (b) Visualisation of vorticity magnitude near the boundary between turbulent and non-turbulent regions. Three yellow lines denote the isolines of  $\omega/\langle\omega\rangle = \omega_{th}$  with  $\omega_{th} = 0.002, 0.005$  and  $0.01$ . The colour contour represents  $\log_{10}(\omega/\langle\omega\rangle)$ . All results are obtained at  $\tau = 0.9T_0$  from case R2200.

2018; Khan & Rao 2023; Ren *et al.* 2024; Li & Wang 2024; Su *et al.* 2024). The vorticity magnitude  $\omega$  exhibits a sharp decrease from turbulent values to near zero across the thin TNTI layer. Consequently, there exists a range of  $\omega_{th}$  for which the volume  $V_\omega$  of the region where  $\omega/\langle\omega\rangle \geq \omega_{th}$  remains relatively constant.

Figure 26(a) illustrates the  $\omega_{th}$  dependence of the normalised volume  $\hat{V}_\omega = V_\omega/L_x L_y L_z$  and its derivative  $-d\hat{V}_\omega/d(\log_{10} \omega_{th})$  in R2200, where  $L_x L_y L_z$  denotes the computational domain volume. As  $\omega_{th}$  decreases from  $10^1$ ,  $\hat{V}_\omega$  increases, indicating the detection of more turbulent fluid. For  $10^{-3} \leq \omega_{th} \leq 10^{-2}$ ,  $\hat{V}_\omega$  remains nearly constant, as confirmed by the small values of  $-d\hat{V}_\omega/d(\log_{10} \omega_{th})$ . This plateau region represents the optimal range for  $\omega_{th}$  in detecting turbulent fluid. When  $\omega_{th}$  falls below  $10^{-4}$ ,  $\hat{V}_\omega$  increases again due to numerical errors. This characteristic profile of  $\hat{V}_\omega(\omega_{th})$  is typical for intermittent turbulent flows (Taveira *et al.* 2013). In this study,  $\omega_{th} = 0.01$  is adopted to identify turbulent fluid.

Figure 26(b) provides a two-dimensional visualisation of vorticity magnitude near the isosurface of  $\omega/\langle\omega\rangle = 0.01$ . The yellow lines represent isolines of  $\omega/\langle\omega\rangle = \omega_{th}$  for  $\omega_{th} = 0.002, 0.005$  and  $0.01$ . All these lines effectively demarcate the boundary between rotational and irrotational regions. The threshold  $\omega_{th}$  is utilised solely to determine perturbation locations. The differences among the three lines are on the order of a few Kolmogorov scales, leading to nearly identical distributions of perturbations, with wavelengths normalised by the Kolmogorov scale ranging between 8 and 210. Other studies on the TNTI layer have also examined the threshold dependence of conditional statistics calculated as a function of the distance from the isosurface of  $\omega$  (Watanabe *et al.* 2018, 2019). When  $\omega_{th}$  is determined using the method based on  $V_\omega$ , the conditional statistics are insensitive to  $\omega_{th}$ , provided that  $\omega_{th}$  is chosen from the plateau region in the plot of  $V_\omega(\omega_{th})$ .

A similar threshold is applied to the passive scalar  $\phi$  to delineate the boundary of the scalar mixing layers. This study focuses on the boundary facing the non-turbulent fluid, identified as the isosurface of  $\phi = \phi_{th}$ . Analogous to the vorticity variation across the TNTI layer, the passive scalar decreases sharply from the interior to the exterior of the scalar mixing layer. Therefore, the outer boundary of the scalar mixing layer can be defined by the isosurface corresponding to a small scalar value (Bilger *et al.* 1976; Kim & Bilger 2007). The method used to determine the vorticity threshold  $\omega_{th}$  is similarly applied to the passive scalar. The value of  $\phi_{th}$  is determined by examining the volume  $V_\phi$  of fluid where  $\phi \geq \phi_{th}$

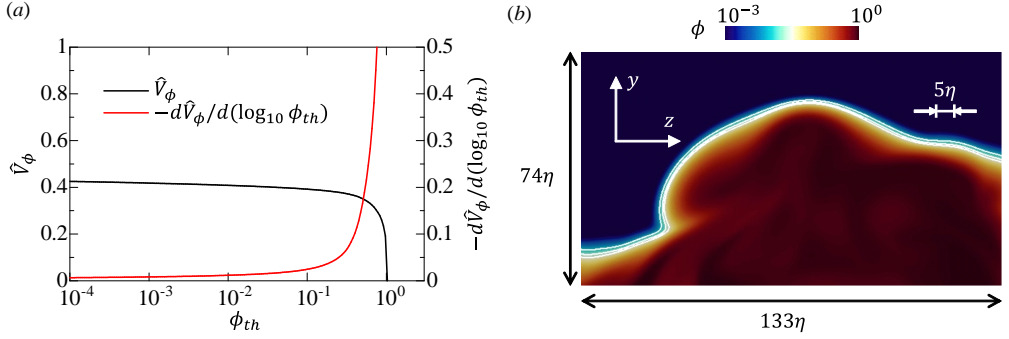


Figure 27: (a) The volume  $V_\phi$  enclosed by the scalar isosurface of  $\phi = \phi_{th}$ , evaluated as a function of  $\phi_{th}$ . This volume is normalised as  $\hat{V}_\phi = V_\phi/L_x L_y L_z$ . (b) Visualisation of the scalar field  $\phi$  near the boundary of the scalar mixing layer. Three white lines represent the isolines of  $\phi = \phi_{th}$  with  $\phi_{th} = 0.01, 0.02$  and  $0.03$ . The colour contour depicts  $\log_{10} \phi$ . All results are obtained at  $\tau = 0.9T_0$  from case R2200. The visualised region is the same as in figure 26.

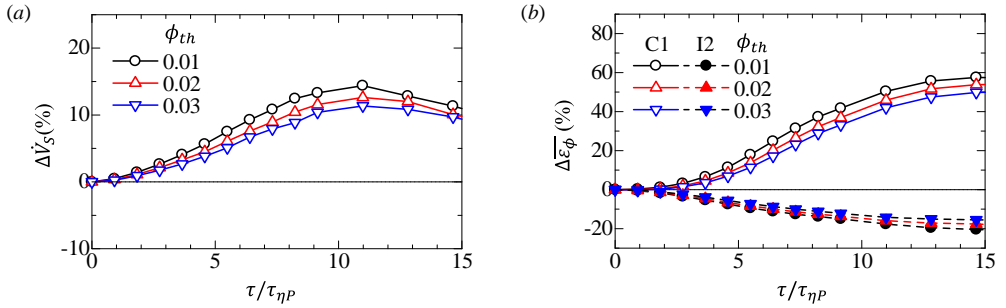


Figure 28: (a) Increase ratio in  $\hat{V}_S$  due to external perturbations, denoted as  $\Delta\hat{V}_S$ . (b) Relative changes in mean scalar dissipation rate, denoted as  $\Delta\overline{\varepsilon}_\phi$ , at different positions along the  $\zeta_I$  coordinate defined in figure 12. The results of R350L30e are compared for  $\phi_{th} = 0.01, 0.02$  and  $0.03$ .

1143 as a function of  $\phi_{th}$ . Figure 27(a) plots the normalised volume  $\hat{V}_\phi = V_\phi/L_x L_y L_z$  against  
 1144  $\phi_{th}$ . As  $\phi_{th}$  decreases,  $\hat{V}_\phi$  becomes less sensitive to changes in  $\phi_{th}$ , as indicated by the  
 1145 reduction in  $-d\hat{V}_\phi/d(\log_{10} \phi_{th})$ . This study adopts  $\phi_{th} = 0.02$ , around which  $\hat{V}_\phi$  shows  
 1146 minimal variation with  $\phi_{th}$ . Figure 27(b) visualises the isolines for  $\phi_{th} = 0.01, 0.02$  and  
 1147  $0.03$ . As anticipated from the  $\phi_{th}$  dependence of  $\hat{V}_\phi$ , small changes in  $\phi_{th}$  have negligible  
 1148 impact on the location of scalar isolines. In addition, the location and geometry of the scalar  
 1149 isoline closely resemble those of the vorticity isosurface in figure 26(b). Figure 28 presents  
 1150 the relative changes due to perturbations in the growth rate of the scalar mixing layer,  $\Delta\hat{V}_S$ ,  
 1151 and the mean scalar dissipation rate near the interface,  $\Delta\overline{\varepsilon}_\phi$ , for three values of  $\phi_{th}$ . Similar  
 1152 behaviors are observed for these quantities regardless of  $\phi_{th}$ . Positive values of  $\Delta\hat{V}_S$  indicate  
 1153 an increased growth rate of the scalar mixing layer. Region C1, defined in figure 12, exhibits  
 1154 positive  $\Delta\overline{\varepsilon}_\phi$ , confirming enhanced mixing at small scales due to the perturbations. The  
 1155 mean scalar dissipation rate decreases in I2 with perturbations, as indicated by  $\Delta\overline{\varepsilon}_\phi < 0$ , due  
 1156 to the reduced scalar gradient within the interfacial layer. Quantitatively, a 50% increase or  
 1157 decrease in  $\phi_{th}$  from  $\phi_{th} = 0.02$  leads to less than a 10% change in  $\Delta\hat{V}_S$  and  $\Delta\overline{\varepsilon}_\phi$ . Thus, the

conclusions regarding the effects of perturbations on scalar mixing remain consistent across these values of  $\phi_{th}$ .

## REFERENCES

- ABREU, H., PINHO, F. T. & DA SILVA, C. B. 2022 Turbulent entrainment in viscoelastic fluids. *J. Fluid Mech.* **934**, A36.
- ANTONIA, R. A. 1981 Conditional sampling in turbulence measurement. *Annu. Rev. Fluid Mech.* **13**, 131–156.
- BENARD, N., BONNET, J.-P., TOUCHARD, G. & MOREAU, E. 2008 Flow control by dielectric barrier discharge actuators: jet mixing enhancement. *AIAA J.* **46** (9), 2293–2305.
- BHATT, K. & TSUJI, Y. 2021 Identification of vortex structures in flow fields using tomographic PIV method. *J. Fluid Sci. Tech.* **16** (3), JFST0018.
- BILGER, R. W. 2004 Some aspects of scalar dissipation. *Flow, Turbul. Combust.* **72** (2-4), 93–114.
- BILGER, R. W., ANTONIA, R. A. & SREENIVASAN, K. R. 1976 Determination of intermittency from the probability density function of a passive scalar. *Phys. Fluids* **19** (10), 1471–1474.
- BILGER, R. W., SAETRAN, L. R. & KRISHNAMOORTHY, L. V. 1991 Reaction in a scalar mixing layer. *J. Fluid Mech.* **233**, 211–242.
- BISSET, D. K., HUNT, J. C. R. & ROGERS, M. M. 2002 The turbulent/non-turbulent interface bounding a far wake. *J. Fluid Mech.* **451**, 383–410.
- BLAKELEY, B. C., OLSON, B. J. & RILEY, J. J. 2022 Self-similarity of scalar isosurface area density in a temporal mixing layer. *J. Fluid Mech.* **951**, A44.
- BLAKELEY, B. C., OLSON, B. J. & RILEY, J. J. 2023 On the evolution of scalar iso-surface area density in a turbulent mixing layer. *J. Fluid Mech.* **966**, A33.
- BREDA, M. & BUXTON, O. R. H. 2019 Behaviour of small-scale turbulence in the turbulent/non-turbulent interface region of developing turbulent jets. *J. Fluid Mech.* **879**, 187–216.
- BRITTER, R. E., HUNT, J. C. R. & MUMFORD, J. C. 1979 The distortion of turbulence by a circular cylinder. *J. Fluid Mech.* **92** (2), 269–301.
- BUXTON, O. R. H., BREDA, M. & DHALL, K. 2019 Importance of small-scale anisotropy in the turbulent/nonturbulent interface region of turbulent free shear flows. *Phys. Rev. Fluids* **4** (3), 034603.
- BUXTON, O. R. H. & GANAPATHISUBRAMANI, B. 2010 Amplification of enstrophy in the far field of an axisymmetric turbulent jet. *J. Fluid Mech.* **651**, 483–502.
- CARROLL, P. L. & BLANQUART, G. 2013 A proposed modification to Lundgren’s physical space velocity forcing method for isotropic turbulence. *Phys. Fluids* **25** (10), 105114.
- CATTAFESTA III, L. N. & SHEPLAK, M. 2011 Actuators for active flow control. *Annu. Rev. Fluid Mech.* **43**, 247–272.
- CHEN, C.-H. P. & BLACKWELDER, R. F. 1978 Large-scale motion in a turbulent boundary layer: a study using temperature contamination. *J. Fluid Mech.* **89** (1), 1–31.
- CHEN, J. & BUXTON, O. R. H. 2023 Spatial evolution of the turbulent/turbulent interface geometry in a cylinder wake. *J. Fluid Mech.* **969**, A4.
- CHEN, X., CHUNG, Y. M. & WAN, M. 2021 The uniform-momentum zones and internal shear layers in turbulent pipe flows at Reynolds numbers up to  $re_\tau = 1000$ . *Int. J. Heat Fluid Flow* **90**, 108817.
- CIMARELLI, A., COCCONI, G., FROHNAPFEL, B. & DE ANGELIS, E. 2015 Spectral enstrophy budget in a shear-less flow with turbulent/non-turbulent interface. *Phys. Fluids* **27** (12), 125106.
- CORCOS, G. M. & LIN, S. J. 1984 The mixing layer: deterministic models of a turbulent flow. Part 2. The origin of the three-dimensional motion. *J. Fluid Mech.* **139**, 67–95.
- DAS, R. & GIRIMAJI, S. S. 2020 Characterization of velocity-gradient dynamics in incompressible turbulence using local streamline geometry. *J. Fluid Mech.* **895**, A5.
- DIMOTAKIS, P. E. 2005 Turbulent mixing. *Annu. Rev. Fluid Mech.* **37**, 329–356.
- DOGAN, E., HANSON, R. E. & GANAPATHISUBRAMANI, B. 2016 Interactions of large-scale free-stream turbulence with turbulent boundary layers. *J. Fluid Mech.* **802**, 79–107.
- EISMA, J., WESTERWEEEL, J., OOMS, G. & ELSINGA, G. E. 2015 Interfaces and internal layers in a turbulent boundary layer. *Phys. Fluids* **27** (5), 055103.
- ELSINGA, G. E., ISHIHARA, T., GOUDAR, M. V., DA SILVA, C. B. & HUNT, J. C. R. 2017 The scaling of straining motions in homogeneous isotropic turbulence. *J. Fluid Mech.* **829**, 31–64.

- 1210 ELSINGA, G. E. & MARUSIC, I. 2010 Universal aspects of small-scale motions in turbulence. *J. Fluid Mech.*  
1211 **662**, 514–539.
- 1212 ELSINGA, G. E. & DA SILVA, C. B. 2019 How the turbulent/non-turbulent interface is different from internal  
1213 turbulence. *J. Fluid Mech.* **866**, 216–238.
- 1214 ENOKI, R., WATANABE, T. & NAGATA, K. 2023 Statistical properties of shear and nonshear velocity  
1215 components in isotropic turbulence and turbulent jets. *Phys. Rev. Fluids* **8** (10), 104602.
- 1216 ER, S., LAVAL, J.-P. & VASSILICOS, J. C. 2023 Length scales and the turbulent/non-turbulent interface of a  
1217 temporally developing turbulent jet. *J. Fluid Mech.* **970**, A33.
- 1218 FAN, D., XU, J., YAO, M. X. & HICKEY, J.-P. 2019 On the detection of internal interfacial layers in turbulent  
1219 flows. *J. Fluid Mech.* **872**, 198–217.
- 1220 FISCALETTI, D., BUXTON, O. R. H. & ATTILI, A. 2021 Internal layers in turbulent free-shear flows. *Phys. Rev.*  
1221 *Fluids* **6** (3), 034612.
- 1222 FISCALETTI, D., RAGNI, D., OVERMARS, E. F. J., WESTERWEEL, J. & ELSINGA, G. E. 2022 Tomographic  
1223 long-distance  $\mu$ PIV to investigate the small scales of turbulence in a jet at high Reynolds number.  
1224 *Exp. Fluids* **63** (1), 9.
- 1225 FOX, R. O. 2003 *Computational Models for Turbulent Reacting Flows*. Cambridge Univ. Pr.
- 1226 GAMPERT, M., BOSCHUNG, J., HENNIG, F., GAUDING, M. & PETERS, N. 2014 The vorticity versus the scalar  
1227 criterion for the detection of the turbulent/non-turbulent interface. *J. Fluid Mech.* **750**, 578–596.
- 1228 GHIRA, A. A., ELSINGA, G. E. & DA SILVA, C. B. 2022 Characteristics of the intense vorticity structures in  
1229 isotropic turbulence at high Reynolds numbers. *Phys. Rev. Fluids* **7** (10), 104605.
- 1230 GUL, M., ELSINGA, G. E. & WESTERWEEL, J. 2020 Internal shear layers and edges of uniform momentum  
1231 zones in a turbulent pipe flow. *J. Fluid Mech.* **901**, A10.
- 1232 HANCOCK, P. E. & BRADSHAW, P. 1989 Turbulence structure of a boundary layer beneath a turbulent free  
1233 stream. *J. Fluid Mech.* **205**, 45–76.
- 1234 HAYASHI, M., WATANABE, T. & NAGATA, K. 2021a Characteristics of small-scale shear layers in a temporally  
1235 evolving turbulent planar jet. *J. Fluid Mech.* **920**, A38.
- 1236 HAYASHI, M., WATANABE, T. & NAGATA, K. 2021b The relation between shearing motions and the  
1237 turbulent/non-turbulent interface in a turbulent planar jet. *Phys. Fluids* **33** (5), 055126.
- 1238 HEISEL, M., DE SILVA, C. M., HUTCHINS, N., MARUSIC, I. & GUALA, M. 2021 Prograde vortices, internal  
1239 shear layers and the Taylor microscale in high-Reynolds-number turbulent boundary layers. *J. Fluid*  
1240 *Mech.* **920**, A52.
- 1241 HILL, J. C. 1976 Homogeneous turbulent mixing with chemical reaction. *Annu. Rev. Fluid Mech.* **8**, 135–161.
- 1242 HOLZNER, M. & LÜTHI, B. 2011 Laminar superlayer at the turbulence boundary. *Phys. Rev. Lett.* **106** (13),  
1243 134503.
- 1244 HORIUTI, K. & TAKAGI, Y. 2005 Identification method for vortex sheet structures in turbulent flows. *Phys.*  
1245 *Fluids* **17** (12), 121703.
- 1246 HUANG, J., BURRIDGE, H. C. & VAN REEUWIJK, M. 2023 Local entrainment across a TNTI and a TTI in a  
1247 turbulent forced fountain. *J. Fluid Mech.* **977**, A13.
- 1248 IOVIENO, M., DI SAVINO, S., GALLANA, L. & TORDELLA, D. Y. 2014 Mixing of a passive scalar across a  
1249 thin shearless layer: concentration of intermittency on the sides of the turbulent interface. *J. Turbul.*  
1250 **15** (5), 311–334.
- 1251 ISHIHARA, T., KANEDA, Y. & HUNT, J. C. R. 2013 Thin shear layers in high Reynolds number turbulence–DNS  
1252 results. *Flow, Turbul. Combust.* **91** (4), 895–929.
- 1253 ITO, Y., MIURA, K., SAKAI, Y. & IWANO, K. 2018 Enhancement and suppression of mixing and diffusion in  
1254 an axisymmetric jet by half delta-wing tabs. *Int. J. Heat Mass Transfer* **118**, 1218–1230.
- 1255 IYER, K. P., SCHUMACHER, J., SREENIVASAN, K. R. & YEUNG, P. K. 2020 Fractal iso-level sets in high-  
1256 reynolds-number scalar turbulence. *Phys. Rev. Fluids* **5** (4), 044501.
- 1257 JAHANBAKSHI, R. & MADNIA, C. K. 2016 Entrainment in a compressible turbulent shear layer. *J. Fluid*  
1258 *Mech.* **797**, 564–603.
- 1259 JAHANBAKSHI, R., VAGHEFI, N. S. & MADNIA, C. K. 2015 Baroclinic vorticity generation near the  
1260 turbulent/non-turbulent interface in a compressible shear layer. *Phys. Fluids* **27** (10), 105105.
- 1261 JIMÉNEZ, J. & WRAY, A. A. 1998 On the characteristics of vortex filaments in isotropic turbulence. *J. Fluid*  
1262 *Mech.* **373**, 255–285.
- 1263 JIMÉNEZ, J., WRAY, A. A., SAFFMAN, P. G. & ROGALLO, R. S. 1993 The structure of intense vorticity in  
1264 isotropic turbulence. *J. Fluid Mech.* **255**, 65–90.
- 1265 JOOSS, Y., LI, L., BRACCHI, T. & HEARST, R. J. 2021 Spatial development of a turbulent boundary layer  
1266 subjected to freestream turbulence. *J. Fluid Mech.* **911**, A4.



- KANG, H. S. & MENEVEAU, C. 2008 Experimental study of an active grid-generated shearless mixing layer and comparisons with large-eddy simulation. *Phys. Fluids* **20** (12), 125102.
- KANG, S.-J., TANAHASHI, M. & MIYAUCHI, T. 2007 Dynamics of fine scale eddy clusters in turbulent channel flows. *J. Turbul.* **8**, N52.
- KANKANWADI, K. S. & BUXTON, O. R. H. 2020 Turbulent entrainment into a cylinder wake from a turbulent background. *J. Fluid Mech.* **905**, A35.
- KATO, H., TAKAMURE, K. & UCHIYAMA, T. 2022 Characteristics of vortex shedding in the wake of a sphere with a uniaxial through-hole. *AIP Adv.* **12** (10), 105112.
- KHAN, J. R. & RAO, S. 2023 Properties of the turbulent/non-turbulent layer of a turbulent Boussinesq plume: A study using direct numerical simulation. *Phys. Fluids* **35** (5), 055140.
- KIM, S. H. & BILGER, R. W. 2007 Iso-surface mass flow density and its implications for turbulent mixing and combustion. *J. Fluid Mech.* **590**, 381–409.
- KOHAN, K. F. & GASKIN, S. 2020 The effect of the geometric features of the turbulent/non-turbulent interface on the entrainment of a passive scalar into a jet. *Phys. Fluids* **32** (9), 095114.
- KOHAN, K. F. & GASKIN, S. J. 2022 On the scalar turbulent/turbulent interface of axisymmetric jets. *J. Fluid Mech.* **950**, A32.
- KOLÁŘ, V. 2007 Vortex identification: New requirements and limitations. *Int. J. Heat Fluid Flow* **28** (4), 638–652.
- KOZUL, M., HEARST, R. J., MONTY, J. P., GANAPATHISUBRAMANI, B. & CHUNG, D. 2020 Response of the temporal turbulent boundary layer to decaying free-stream turbulence. *J. Fluid Mech.* **896**, A11.
- KRONBORG, J. & HOFFMAN, J. 2023 The triple decomposition of the velocity gradient tensor as a standardized real Schur form. *Phys. Fluids* **35** (3), 031703.
- KWON, Y. S., PHILIP, J., DE SILVA, C. M., HUTCHINS, N. & MONTY, J. P. 2014 The quiescent core of turbulent channel flow. *Journal of Fluid Mechanics* **751**, 228–254.
- LI, S. & WANG, J. 2024 Entrainment of the shear layer separated from a wall-mounted fence. *J. Fluid Mech.* **999**, A6.
- LIU, C., GAO, Y., TIAN, S. & DONG, X. 2018 Rortex-A new vortex vector definition and vorticity tensor and vector decompositions. *Phys. Fluids* **30** (3), 035103.
- LIU, P., DUAN, H. & ZHAO, W. 2009 Numerical investigation of hot air recirculation of air-cooled condensers at a large power plant. *Appl. Therm. Eng.* **29** (10), 1927–1934.
- LONGMIRE, E. K., EATON, J. K. & ELKINS, C. J. 1992 Control of jet structure by crown-shaped nozzles. *AIAA J.* **30** (2), 505–512.
- MATSUSHIMA, T., NAGATA, K. & WATANABE, T. 2021 Wavelet analysis of shearless turbulent mixing layer. *Phys. Fluids* **33** (2), 025109.
- MENEVEAU, C. & SREENIVASAN, K. R. 1990 Interface dimension in intermittent turbulence. *Phys. Rev. A* **41** (4), 2246.
- MISTRY, D., DAWSON, J. R. & KERSTEIN, A. R. 2018 The multi-scale geometry of the near field in an axisymmetric jet. *J. Fluid Mech.* **838**, 501–515.
- MISTRY, D., PHILIP, J., DAWSON, J. R. & MARUSIC, I. 2016 Entrainment at multi-scales across the turbulent/non-turbulent interface in an axisymmetric jet. *J. Fluid Mech.* **802**, 690–725.
- MORINISHI, Y., LUND, T. S., VASILYEV, O. V. & MOIN, P. 1998 Fully conservative higher order finite difference schemes for incompressible flow. *J. Comput. Phys.* **143** (1), 90–124.
- MOURI, H., HORI, A. & KAWASHIMA, Y. 2007 Laboratory experiments for intense vortical structures in turbulence velocity fields. *Phys. Fluids* **19** (5), 055101.
- MURLIS, J., TSAI, H. M. & BRADSHAW, P. 1982 The structure of turbulent boundary layers at low Reynolds numbers. *J. Fluid Mech.* **122**, 13–56.
- NAGATA, K., SAKAI, Y. & KOMORI, S. 2011 Effects of small-scale freestream turbulence on turbulent boundary layers with and without thermal convection. *Phys. Fluids* **23** (6), 065111.
- NAGATA, R., WATANABE, T. & NAGATA, K. 2018 Turbulent/non-turbulent interfaces in temporally evolving compressible planar jets. *Phys. Fluids* **30** (10), 105109.
- NAGATA, R., WATANABE, T., NAGATA, K. & DA SILVA, C. B. 2020a Triple decomposition of velocity gradient tensor in homogeneous isotropic turbulence. *Comput. Fluids* **198**, 104389.
- NAGATA, T., NOGUCHI, A., KUSAMA, K., NONOMURA, T., KOMURO, A., ANDO, A. & ASAI, K. 2020b Experimental investigation on compressible flow over a circular cylinder at Reynolds number of between 1000 and 5000. *J. Fluid Mech.* **893**, A13.
- NAKAMURA, K., MATSUSHIMA, T., ZHENG, Y., NAGATA, K. & WATANABE, T. 2022 Large-and small-scale

- characteristics in a temporally developing shearless turbulent mixing layer. *Phys. Fluids* **34** (11), 115117.
- NAKAMURA, K., WATANABE, T. & NAGATA, K. 2023 Turbulent/turbulent interfacial layers of a shearless turbulence mixing layer in temporally evolving grid turbulence. *Phys. Fluids* **35** (4), 045117.
- NEAMTU-HALIC, M. M., KRUG, D., MOLLICONE, J.-P., VAN REEUWIJK, M., HALLER, G. & HOLZNER, M. 2020 Connecting the time evolution of the turbulence interface to coherent structures. *J. Fluid Mech.* **898**, A3.
- PAPAMOSCHOU, D. & ROSHKO, A. 1988 The compressible turbulent shear layer: an experimental study. *J. Fluid Mech.* **197**, 453–477.
- PASSOT, T., POLITANO, H., SULEM, P. L., ANGILELLA, J. R. & MENEGUZZI, M. 1995 Instability of strained vortex layers and vortex tube formation in homogeneous turbulence. *J. Fluid Mech.* **282**, 313–338.
- PHILLIPS, O. M. 1955 The irrotational motion outside a free turbulent boundary. In *Proc. Cambridge Philos. Soc.*, vol. 51, pp. 220–229. Cambridge Univ. Press.
- PIROZZOLI, S., BERNARDINI, M. & GRASSO, F. 2010 On the dynamical relevance of coherent vortical structures in turbulent boundary layers. *J. Fluid Mech.* **648**, 325–349.
- POPE, S. B. 1988 The evolution of surfaces in turbulence. *Int. J. Eng. Sci.* **26** (5), 445–469.
- VAN REEUWIJK, M. & HOLZNER, M. 2014 The turbulence boundary of a temporal jet. *J. Fluid Mech.* **739**, 254–275.
- REN, J., WANG, H., LUO, K. & FAN, J. 2024 Investigation of entrainment and its effect on flame stabilization in a turbulent high Karlovitz number premixed jet flame using direct numerical simulation. *Flow, Turbul. Combust.* **112**, 537–556.
- RUETSCH, G. R. & MAXEY, M. R. 1991 Small-scale features of vorticity and passive scalar fields in homogeneous isotropic turbulence. *Phys. Fluids* **3** (6), 1587–1597.
- RUETSCH, G. R. & MAXEY, M. R. 1992 The evolution of small-scale structures in homogeneous isotropic turbulence. *Phys. Fluids* **4** (12), 2747–2760.
- SADEGHI, H., LAVOIE, P. & POLLARD, A. 2014 The effect of Reynolds number on the scaling range along the centreline of a round turbulent jet. *J. Turbul.* **15** (6), 335–349.
- SAKURAI, Y. & ISHIHARA, T. 2018 Relationships between small-scale fluid motions and inertial particle clustering in turbulence. *J. Phys. Soc. Japan* **87** (9), 093401.
- SHARP, N. S., NEUSCAMMAN, S. & WARHAFT, Z. 2009 Effects of large-scale free stream turbulence on a turbulent boundary layer. *Phys. Fluids* **21** (9), 095105.
- SIGGIA, E. D. 1981 Numerical study of small-scale intermittency in three-dimensional turbulence. *J. Fluid Mech.* **107**, 375–406.
- DA SILVA, C. B., DOS REIS, R. J. N. & PEREIRA, J. C. F. 2011 The intense vorticity structures near the turbulent/non-turbulent interface in a jet. *J. Fluid Mech.* **685**, 165–190.
- DA SILVA, C. B., HUNT, J. C. R., EAMES, I. & WESTERWEEL, J. 2014 Interfacial layers between regions of different turbulence intensity. *Annu. Rev. Fluid Mech.* **46**, 567–590.
- DA SILVA, C. B. & PEREIRA, J. C. F. 2008 Invariants of the velocity-gradient, rate-of-strain, and rate-of-rotation tensors across the turbulent/nonturbulent interface in jets. *Phys. Fluids* **20** (5), 055101.
- DA SILVA, C. B. & TAVEIRA, R. R. 2010 The thickness of the turbulent/nonturbulent interface is equal to the radius of the large vorticity structures near the edge of the shear layer. *Phys. Fluids* **22** (12), 121702.
- SILVA, T. S. & DA SILVA, C. B. 2017 The behaviour of the scalar gradient across the turbulent/non-turbulent interface in jets. *Phys. Fluids* **29** (8), 085106.
- SREENIVASAN, K. R., RAMSHANKAR, R. & MENEVEAU, C. H. 1989 Mixing, entrainment and fractal dimensions of surfaces in turbulent flows. *Proc. R. Soc. Lond. A* **421** (1860), 79–108.
- SU, S., LONG, Y., WANG, J. & LI, X. 2024 Investigations on the turbulent/non-turbulent interface in supersonic compressible plate turbulent boundary layer. *J. Fluid Mech.* **988**, A30.
- TAVEIRA, R. R., DIOGO, J. S., LOPES, D. C. & DA SILVA, C. B. 2013 Lagrangian statistics across the turbulent-nonturbulent interface in a turbulent plane jet. *Phys. Rev. E* **88** (4), 043001.
- TAVEIRA, R. R. & DA SILVA, C. B. 2013 Kinetic energy budgets near the turbulent/nonturbulent interface in jets. *Phys. Fluids* **25**, 015114.
- TAVEIRA, R. R. & DA SILVA, C. B. 2014 Characteristics of the viscous superlayer in shear free turbulence and in planar turbulent jets. *Phys. Fluids* **26** (2), 021702.
- TEIXEIRA, M. A. C. & DA SILVA, C. B. 2012 Turbulence dynamics near a turbulent/non-turbulent interface. *J. Fluid Mech.* **695**, 257–287.
- VEERAVALLI, S. & WARHAFT, Z. 1989 The shearless turbulence mixing layer. *J. Fluid Mech.* **207**, 191–229.

- VINCENT, A. & MENEGUZZI, M. 1994 The dynamics of vorticity tubes in homogeneous turbulence. *J. Fluid Mech.* **258**, 245–254.
- WATANABE, T. 2024a Efficient enhancement of turbulent entrainment by small-scale shear instability. *J. Fluid Mech.* **988**, A20.
- WATANABE, T. 2024b Enhancement of passive scalar mixing in a shear-free turbulent front. In *IUTAM Symposium on Turbulent/Non-Turbulent Interface in Turbulent Shear Flows*, pp. 79–93. Springer.
- WATANABE, T., JAULINO, R., TAVEIRA, R. R., DA SILVA, C. B., NAGATA, K. & SAKAI, Y. 2017 Role of an isolated eddy near the turbulent/non-turbulent interface layer. *Phys. Rev. Fluids* **2** (9), 094607.
- WATANABE, T., MORI, T., ISHIZAWA, K. & NAGATA, K. 2024 Scale dependence of local shearing motion in decaying turbulence generated by multiple-jet interaction. *J. Fluid Mech.* **997**, A14.
- WATANABE, T. & NAGATA, K. 2023 The response of small-scale shear layers to perturbations in turbulence. *J. Fluid Mech.* **963**, A31.
- WATANABE, T., NAITO, T., SAKAI, Y., NAGATA, K. & ITO, Y. 2015a Mixing and chemical reaction at high schmidt number near turbulent/nonturbulent interface in planar liquid jet. *Phys. Fluids* **27** (3), 035114.
- WATANABE, T., RILEY, J. J. & NAGATA, K. 2016a Effects of stable stratification on turbulent/nonturbulent interfaces in turbulent mixing layers. *Phys. Rev. Fluids* **1** (4), 044301.
- WATANABE, T., SAKAI, Y., NAGATA, K. & ITO, Y. 2016b Large eddy simulation study of turbulent kinetic energy and scalar variance budgets and turbulent/non-turbulent interface in planar jets. *Fluid Dyn. Res.* **48** (2), 021407.
- WATANABE, T., SAKAI, Y., NAGATA, K., ITO, Y. & HAYASE, T. 2014a Enstrophy and passive scalar transport near the turbulent/non-turbulent interface in a turbulent planar jet flow. *Phys. Fluids* **26** (10), 105103.
- WATANABE, T., SAKAI, Y., NAGATA, K., ITO, Y. & HAYASE, T. 2014b Reactive scalar field near the turbulent/non-turbulent interface in a planar jet with a second-order chemical reaction. *Phys. Fluids* **26** (10), 105111.
- WATANABE, T., SAKAI, Y., NAGATA, K., ITO, Y. & HAYASE, T. 2015b Turbulent mixing of passive scalar near turbulent and non-turbulent interface in mixing layers. *Phys. Fluids* **27** (8), 085109.
- WATANABE, T., SAKAI, Y., NAGATA, K., TERASHIMA, O., SUZUKI, H., HAYASE, T. & ITO, Y. 2013 Visualization of turbulent reactive jet by using direct numerical simulation. *Int. J. Model. Simul. Sci. Comput.* **4**, 1341001.
- WATANABE, T., DA SILVA, C. B. & NAGATA, K. 2019 Non-dimensional energy dissipation rate near the turbulent/non-turbulent interfacial layer in free shear flows and shear free turbulence. *J. Fluid Mech.* **875**, 321–344.
- WATANABE, T., DA SILVA, C. B., SAKAI, Y., NAGATA, K. & HAYASE, T. 2016c Lagrangian properties of the entrainment across turbulent/non-turbulent interface layers. *Phys. Fluids* **28** (3), 031701.
- WATANABE, T., TANAKA, K. & NAGATA, K. 2020 Characteristics of shearing motions in incompressible isotropic turbulence. *Phys. Rev. Fluids* **5** (7), 072601(R).
- WATANABE, T., ZHANG, X. & NAGATA, K. 2018 Turbulent/non-turbulent interfaces detected in DNS of incompressible turbulent boundary layers. *Phys. Fluids* **30** (3), 035102.
- WESTERWEL, J., FUKUSHIMA, C., PEDERSEN, J. M. & HUNT, J. C. R. 2009 Momentum and scalar transport at the turbulent/non-turbulent interface of a jet. *J. Fluid Mech.* **631**, 199–230.
- WOLF, M., LÜTHI, B., HOLZNER, M., KRUG, D., KINZELBACH, W. & TSINOBER, A. 2012 Investigations on the local entrainment velocity in a turbulent jet. *Phys. Fluids* **24** (10), 105110.
- WU, X., WALLACE, J. M. & HICKEY, J.-P. 2019 Boundary layer turbulence and freestream turbulence interface, turbulent spot and freestream turbulence interface, laminar boundary layer and freestream turbulence interface. *Phys. Fluids* **31** (4), 045104.
- XU, C. & LONG, Y. & GUANG WANG, J. 2023 Entrainment mechanism of turbulent synthetic jet flow. *J. Fluid Mech.* **958**, A31.
- ZAMAN, K. B. M. Q., REEDER, M. F. & SAMIMY, M. 1994 Control of an axisymmetric jet using vortex generators. *Phys. Fluids* **6** (2), 778–793.
- ZECCHETTO, M., XAVIER, R. P., TEIXEIRA, M. A. C. & DA SILVA, C. B. 2024 Generalized scaling laws for the irrotational motions bordering a turbulent region. *Phys. Rev. E* **109** (6), 065107.
- ZHANG, X., WATANABE, T. & NAGATA, K. 2019 Passive scalar mixing near turbulent/non-turbulent interface in compressible turbulent boundary layers. *Phys. Scr.* **94** (4), 044002.
- ZHANG, X., WATANABE, T. & NAGATA, K. 2023 Reynolds number dependence of the turbulent/non-turbulent interface in temporally developing turbulent boundary layers. *J. Fluid Mech.* **964**, A8.
- ZHDANOV, V. & CHORNY, A. 2011 Development of macro-and micromixing in confined flows of reactive fluids. *Int. J. Heat Mass Transfer* **54** (15-16), 3245–3255.

- 1436 ZHENG, Y., NAGATA, K. & WATANABE, T. 2021 Turbulent characteristics and energy transfer in the far field  
1437 of active-grid turbulence. *Phys. Fluids* **33** (11), 115119.
- 1438 ZHUANG, Y., TAN, H., HUANG, H., LIU, Y. & ZHANG, Y. 2018 Fractal characteristics of turbulent–non-  
1439 turbulent interface in supersonic turbulent boundary layers. *J. Fluid Mech.* **843**, R2.